

Catalysis Science & Technology

Elucidation of Ce/Zr ratio effects on the physical properties and catalytic performance of CuOx/CeyZr1-yO2 catalysts

Journal:	Catalysis Science & Technology
Manuscript ID	CY-ART-08-2024-001012.R1
Article Type:	Paper
Date Submitted by the Author:	15-Oct-2024
Complete List of Authors:	Sifat, Mohammed; Stony Brook University, Materials Science and Chemical Engineering Luchowski, Michal; Stony Brook University, Materials Science and Chemical Engineering Pophali, Amol; Stony Brook University, Department of Materials Science Chemical Engineering Jiang, Wenhui; Stony Brook University, Materials Science and Chemical Engineering Lu, Yunfan; Stony Brook University, Materials Science and Chemical Engineering Kim, Byeongseok; Inha University, Chemistry and Chemical Engineering Kwon, Gihan; Brookhaven National Laboratory, Photon Science Division - National Synchrotron Light Source II Yoon, Kwangsuk; Hanyang University, Earth Resources and Environmental Engineering Kim, Jihun; Ulsan National Institute of Science and Technology, School of Energy and Chemical Engineering An, Kwangjin; UNIST, School of Energy and Chemical Engineering Shim, Sang Eun; Inha University, Chemical Engineering Song, Hocheol; Hanyang University, Kim, Tae Jin; Stony Brook University, Materials Science and Chemical Engineering

SCHOLARONE™ Manuscripts

Elucidation of Ce/Zr ratio effects on the physical properties and catalytic performance of $CuO_x/Ce_vZr_{1-v}O_2$ catalysts

Mohammed Sifat¹, Michal Luchowski¹, Amol Pophali¹, Wenhui Jiang¹, Yunfan Lu¹, Byeongseok Kim², Gihan Kwon³, Kwangsuk Yoon⁴, Jihun Kim⁵, Kwangjin An⁵, Sang Eun Shim², Hocheol Song⁴, Taejin Kim^{1,*}

Prof. Taejin Kim; Email: taejin.kim@stonybrook.edu

¹ Materials Science and Chemical Engineering Department, Stony Brook University, Stony Brook, NY, 11794, U.S.A

² Department of Chemistry and Chemical Engineering, Education and Research Center for Smart Energy and Materials, Inha University, Incheon, 22212, South Korea

³ National Synchrotron Light Source II, Brookhaven National Laboratory, Upton, NY 11973, U.S.A

⁴ Department of Earth Resources and Environmental Engineering, Hanyang University, Seoul 04763, Republic of Korea

⁵ School of Energy and Chemical Engineering, Ulsan National Institute of Science and Technology, Ulsan 44919, Republic of Korea

^{*}Corresponding author

Abstract

Although cerium oxide (CeO₂) is widely used as a catalyst support, its limited defect sites and surface oxygen vacancy/mobility should be improved. The incorporation of zirconium (Zr) in the cerium (Ce) lattice is shown to increase the number of oxygen vacancies and improve catalytic activity. Using a fixed surface density (SD) of copper (~2.3 Cu atoms/nm²) as a surface species, the role of the support ($Ce_vZr_{1-v}O_2$ (y = 1.0, 0.9, 0.6, 0.5, and 0.0)) and defect site effects for CO oxidation reaction were investigated. The spectroscopic (e.g., Raman, XRD, XPS) and microscopic (e.g., SEM-EDX, HR-TEM) characterization techniques were applied to evaluate the defect sites, crystallite size, lattice parameters, chemical composition, oxidation states of elements and microstructure of the catalysts. CO oxidation reaction with varied CO:O2 ratios (1:5, 1:1, and 1:0.5 (stoichiometric)) was used as a model reaction to describe the relationship between the structure and catalytic performance of each catalyst. Based on the characterization results of Ce_vZr_{1-v}O₂ materials, the addition of Zr causes physical and chemical changes to the overall material. The inclusion of Zr into the structure of CeO₂ decreased the overall lattice parameter of the catalyst and increased the number of defect sites. The prepared catalysts were able to reach complete CO conversions (~100%) at low temperature conditions (< 200 °C), each showing varied reaction activity. The difference in CO oxidation activity was then analyzed and related to structure wherein Cu loading, surface oxygen vacancies, reduction-oxidation ability, CuO_x-support interaction and oxygen mobility in the catalyst were the crucial descriptors.

Keywords: Ceria-zirconia, copper oxide, surface density, CO oxidation, structure-activity relationship

1. Introduction

Carbon monoxide (CO) is a dangerous pollutant present in air that can be toxic to humans even at very low concentration levels over 50 ppm, while its lethality quickly increases with increasing concentration past 200 ppm.^{1,2} Due to its toxicity, the catalytic oxidation of CO has been of great interest to a variety of industries for applications including CO gas sensors, filtration in air-purification devices such as respirators, and automotive pollution control systems.³ The role of CO in syngas makeup raises the continuous concern of CO pollutants available due to biomass-derived processes becoming increasingly more favorable in the recent decades for providing fuel and energy needs.⁴ Due to varying concentrations in which CO exists as a pollutant and in reactions, the effective oxidation of CO is necessary under varying temperature and reactant compositions. As such, the need to control CO emissions has become increasingly more apparent throughout the years.

In recent decades, cerium oxide (CeO₂), commonly referred to as ceria, has been widely studied in heterogeneous catalysis due to its high oxygen storage capacity (OSC) and propagation of Ce³⁺ and Ce⁴⁺ redox cycle, helping to avoid catalyst deactivation over time.⁵⁻⁷ It has a face-centered cubic (FCC) structure, and its highly organized lattice network allows for the presence of oxygen vacancies produced by the propagation of the redox processes, leading to increased O₂ adsorption used during CO oxidation.^{8,9} In addition to the CO oxidation, CeO₂-based supports have been applied in a range of fields, including ethanol steam reforming (ESR) for hydrogen production, NO reduction by CO for the removal of NO_x pollutants, and reverse water gas shift (RWGS) for the production of syn-gases.^{5,10,11}

Although CeO₂ has been widely employed in various catalytic reactions, it has been reported that pure CeO₂ has low oxygen defect sites and low thermal stability, resulting in limited

active sites (or OSC) and low specific surface area (SSA) at higher calcination treatment temperatures. 5,12-14 To modify the physicochemical properties of CeO₂, a secondary metal species (e.g., zirconium (Zr), tin (Sn), titanium (Ti), lanthanum (La)) has been incorporated into the lattice to form the Ce_vM_{1-v}O₂ solid solutions.^{5,15-17} Among Ce_vM_{1-v}O₂ materials, Zr doped CeO₂-based catalyst (Ce_vZr_{1-v}O₂) has been extensively studied and used in automotive catalytic converters. ¹⁸-²¹ Compared to CeO₂, Ce_vZr_{1-v}O₂ has showed a higher OSC, SSA and oxygen mobility at similar treatment conditions. ²²⁻²⁷ The incorporation of Zr⁴⁺ in the Ce⁴⁺ lattice can change the structure due to the smaller ionic radius of $Zr^{4+}(0.84 \text{ Å})$ compared to that of $Ce^{4+}(0.97 \text{ Å})$, leading to an overall decrease in the lattice parameter of Ce_vZr_{1-v}O₂. ^{22-24,28} X. Yao et al. reported that CuO_x/Ce_vZr_{1-v}O_v showed relatively better catalytic performance for NO reduction by CO compared to CuO_x/Ce_vSn₁. _vO_x and CuO_x/Ce_vTi_{1-v}O_x, which can be attributed to the gradient of electronegativity between primary and secondary support metals.⁵ Since Zr (1.33) has the lower electronegativity compared to Sn (1.96) and Ti (1.54) in the Ce (1.12)-based solid solution, Cu²⁺ is more likely to gain the electron and become Cu⁺ in CuO_x/Ce_yZr_{1-y}O_x catalyst. Surface Cu species exists in various oxidation states due to direct interaction with the support lattice.⁵ As indicated by the redox equilibrium, $Cu^{2+} + Ce^{3+} \leftrightarrow Cu^{+} + Ce^{4+}$, the presence of Cu^{2+} (or Cu^{+}) could affect the amounts of oxygen vacancies and defect sites due to the change of Ce oxidation state (3+ or 4+).^{5,8} J. Chen et al., studied the effect of the Ce/Zr ratio on the catalytic activity for CH₄ combustion reaction and redox properties.²⁸ The authors reported that Ni/Ce_{0.83}Zr_{0.17}O₂ showed the highest catalytic performance as compared to CeO₂, Ce_{0.17}Zr_{0.83}O₂ and ZrO₂ supported Ni catalysts due to its high OSC, which increases the defect sites, improving the mobility of oxygen species. P. Biswas and D. Kunzru investigated the ethanol steam reforming (ESR) reaction over the series of Ce_vZr_{1-v}O₂

(y = 0, 0.26, 0.59, 0.84 and 1) supported Ni catalysts, and concluded that high reducibility and high OSC of catalysts are related to the high catalytic activity and hydrogen selectivity. 11

It has been reported that platinum group metals (PGMs) have shown high catalytic performance for CO oxidation reaction. Due to their high cost, however, research has been focused on studying alternative highly active non-PGM catalysts. $^{11,29-31}$ L. Zhou et al., studied the effect of TMs (e.g., Cu, Co, Ni, Mn, and Fe) on CO oxidation over the TM_xCeO_{2-x} catalyst and reported that Cu_xCeO_{2-x} showed the highest catalytic activity. 30 The authors concluded that the electronic structure and oxygen vacancies are responsible for the higher catalytic activity. It has been reported that TMs increase the catalytic activity due to the formation of surface defects and the selection of surface TM species is highly dependent on the oxygen vacancy formation energy, E_{vf} , of the metal. 29 Among several TMs, Cu has been shown to have a lower E_{vf} , leading to increased catalytic activity for CO oxidation reaction. 32,33 The addition of a surface species and a secondary metal on the CeO_2 lattice is seen to increase OSC, catalytic activity, and oxygen vacancies. 34,35

Although CeO_2 supported TMO_x catalysts have been studied extensively; to understand the support effect (or interaction between surface species and support), a fixing of surface density (SD, # of surface metal atoms/nm²) should be considered. In the present work, the series of $CuO_x/Ce_yZr_{1-y}O_2$ ($CeO_2:ZrO_2 = 90:10$, 60:40, and 50:50 by weight percent) catalysts with fixed Cu SD. The fixed SD of Cu on the supports allows for the number of copper atoms per given area of support (\sim 2.3 Cu atoms/nm²) to be similar for each catalyst. This allows for the studying of the direct effect of the CeO_2/ZrO_2 ratio on the catalytic activity. To measure the catalytic performance of the synthesized catalysts, CO oxidation as a model reaction was performed: $CO + \frac{1}{2}O_2 \rightarrow CO_2$. A variety of spectroscopic and microscopic characterization techniques, such as ICP, BET, Raman, XRD, SEM-EDX and TEM, were employed to determine the molecular structure of the supports

and supported catalysts. It was found that the incorporation of Zr into the Ce lattice increases defect sites. However, the catalytic performance was not proportional to the increase in defect sites. It was also observed that increasing O_2 feed concentration hinders the activity of the catalysts, with oxygen vacancies playing a larger role in leaner O_2 feed conditions.

2. Experimental Section

2.1 Materials and catalyst preparation

 $Ce_yZr_{1-y}O_2$ (y = 1.0, 0.9, 0.6, 0.5, 0.0) materials were provided by Daiichi Kigenso Kagaku Kogyo (DKK). The preparation of the catalysts involved proprietary company methods using a combination of hydrolysis and co-precipitation methods for formation of various CeO_2 : ZrO_2 mixed-oxide ratios (9:1, 6:4, 5:5) by weight percent. The precursors used for synthesis of the mixed-oxide catalysts were a combination of cerium (IV) hydroxide ($Ce(OH)_4$) and zirconium(IV) oxychloride ($ZrOCl_2$).

Copper (II) acetylacetonate ($Cu(acac)_2$, $Cu(C_5H_7O_2)_2$, $\geq 99.9\%$ trace metals basis) was purchased from Sigma-Aldrich. The $CuO_x/Ce_yZr_{1-y}O_2$ (SD = ~2.3 Cu atoms/nm²) samples were synthesized by one-pot chemical vapor deposition (OP-CVD) method as shown in Fig. 1. The OP-CVD method followed three steps for catalyst synthesis: (I) Pre-mixing: The $Ce_yZr_{1-y}O_2$ and $Cu(acac)_2$ were added to a mortar and mixed for 15 mins. The mixed powder was transferred to an aluminum oxide boat (Sigma-Aldrich), and then the sample was transported into a tubular furnace (Lindberg/Blue M Tube Furnace, Model Number: TF55030A-1). (II) Dispersion: The transported sample was treated at 155°C for 2 hours under flowing of N_2 gas (Airgas, ultra-high purity N_2) at a rate of 20 mL/min. Dispersion temperature conditions were selected using a programmed-TGA method in which the 10% weight loss region of the precursor was determined. (III) Calcination:

Following the dispersion, air (Airgas, dry air: 20% O_2 and 80% N_2) flowing at a rate of about 25 mL/min was used to calcine the sample at 500°C for 4 hours. The synthesized $CuO_x/Ce_yZr_{1-y}O_2$ catalyst was left to cool overnight at room temperature and sieved (500 μ m, Fieldmaster) to ensure a uniform particle size.

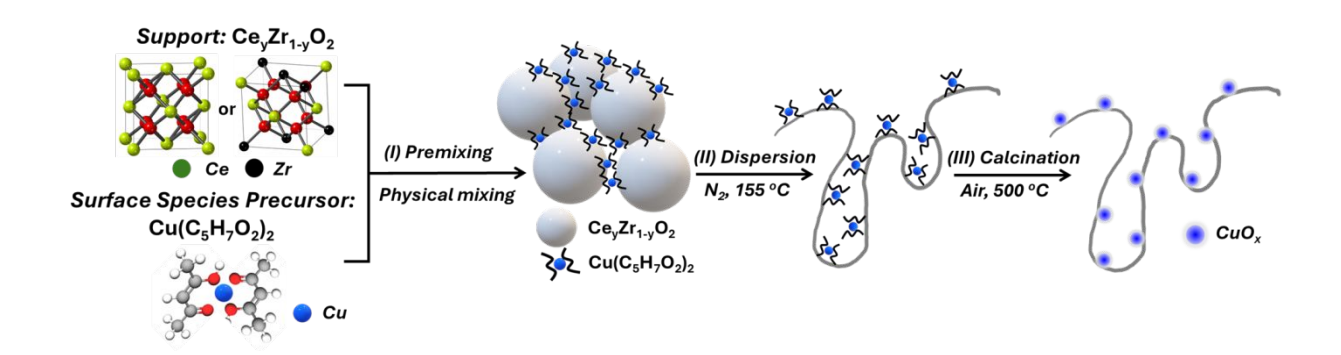


Figure 1. Scheme of the synthesis of copper oxide (CuO_x) on $Ce_yZr_{1-y}O_2$ (y = 1.0, 0.9, 0.6, 0.5, 0.0) supports.

2.2 Catalyst characterization

For the X-ray diffraction (XRD) analysis, the $Ce_yZr_{1-y}O_2$ catalysts underwent synchrotron-x-ray diffraction (S-XRD) (λ = 0.1665 Å) measurement. The processing of the data for conversion from two-dimensional (2D) high energy scattering patterns to one-dimensional (1D) data was done using Dioptas software. The $CuO_x/Ce_yZr_{1-y}O_2$ supported catalysts underwent lab scale XRD using a X'Pert Powder Diffractometer (PANalytical) with a Cu-K α radiation source (λ = 1.5406 Å) operating at 40 kV and 30 mA. The measurement was performed with a diffraction angle 2 θ range of 20–80° at a scanning speed of 1.33°/min.. The Raman spectra of the $Ce_yZr_{1-y}O_2$ and $CuO_x/Ce_yZr_{1-y}O_2$ catalysts were obtained with visible (532 nm, Horiba Xplora Plus Raman microscope) and UV (325 nm, Renishaw inViaTM Raman microscope) excitation at room temperature and ambient pressure. The obtained spectra were displayed within a Raman shift (cm-

1) range of 100 to 2000 cm⁻¹, with spectral acquisition scanning parameters set to 10 accumulations at 10 s/scan. The elemental compositions and associated oxidation states were determined by testing the catalysts for X-ray photoelectron spectroscopy (XPS, Thermo Scientific K-Alpha) with monochromatic Al-K α radiation (hv = 1486.6 eV). The obtained data were analyzed for XPS fitting using Origin software with a Tougaard method baseline and Voigt method curve fitting. N₂adsorption-desorption isotherm curves were obtained at 77 K (-196 °C) using a Micromeritics ASAP 2020 instrument. Prior to the N₂-adsorption-desorption procedures, the samples were degassed at 300°C for 4 hours for removal of any impurities or moisture. The specific surface areas (SSAs) were calculated by the multipoint Brunauer-Emmett-Teller (BET) method. The pore size distribution and the average pore volume of the catalysts were determined by the Barrett, Joyner, and Halenda (BJH) method. Scanning Electron Microscopy coupled with Energy Dispersive Xray (SEM-EDX) analysis was carried out on an EmCrafts Cube II scanning electron microscope (voltage 10 kV). Samples were attached to a specimen holder with carbon tape and coated with platinum. The microstructure of the synthesized catalysts was investigated using the transmission electron microscopy (TEM; JEOL, HEM2100F). The samples were thoroughly dispersed in ethyl alcohol (~1.5 mg/ml) and then mounted on a Ni grid. This sample-mounted Ni grid was further dried under ambient conditions and then used for the measurement. Inductively coupled plasmaoptical emission spectrometry (ICP-OES, Optima 5300DV, PerkinElmer) was used to determine the Cu loading. Prior to the ICP-OES measurement, 0.02 g of the sample was dissolved by 10 mL of nitric acid (70% HNO₃) using a microwave digestion system (ETHOS TC, Milestone).

2.3 Catalytic activity test

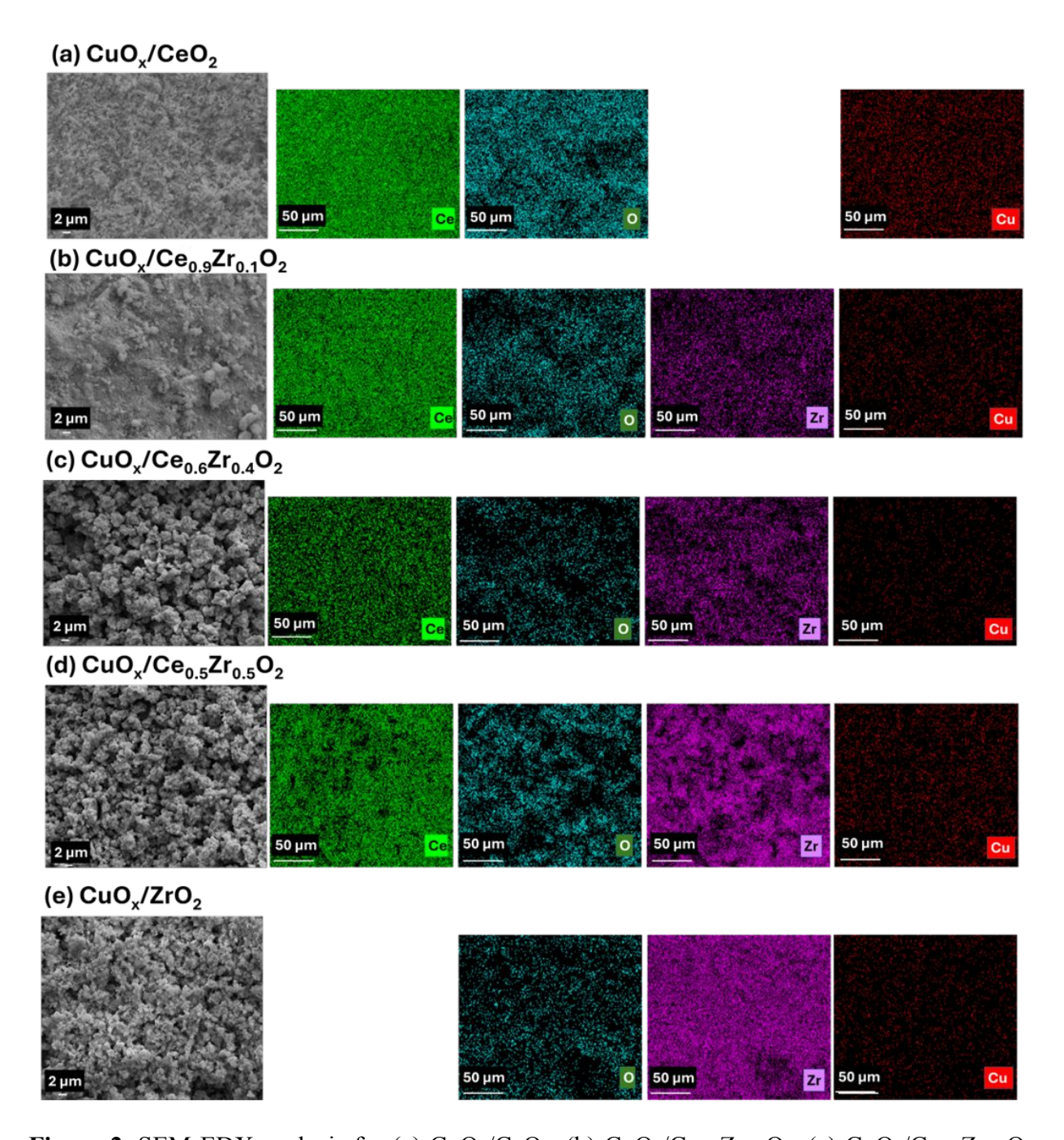
CO oxidation reaction was carried out in a quartz packed bed reactor (Inner diameter (ID) = 7 mm, Outer diameter (OD) = 9.6 mm) and 40 mg of the catalyst was used. The total flow rate

was kept consistent between various activity tests to achieve a gas hourly space velocity (GHSV) value of 75,000 ml/hr/g_{cat}. The sample was pretreated by flowing He (30 mL/min, Airgas, ultrahigh purity) at 500°C (ramping rate of 5°C/min from room temperature) for 30 minutes. Following the pretreatment procedure, the temperature was cooled down to room temperature and the gas composition was switched to the desired reactant compositions. The total flow rate was 50 mL/min and the feed gases were varied with different CO to O₂ ratios: (I) 20 mL/min CO (Airgas, 10% CO with balance He), 10 mL/min O₂ (Airgas, ultra-high purity), and 20 mL/min He (Airgas, ultra-high-purity) for the 1:5 CO to O₂ ratio, (II) 20 mL/min CO, 2 mL/min O₂, and 28 mL/min He for the 1:1 CO to O₂ ratio, and (III) 40 mL/min CO, 2 mL/min O₂, and 8 mL/min He for the 1:0.5 CO to O₂ ratio (stoichiometric). The reactants and products were analyzed by using an on-line gas chromatograph (GC, Trace 1300 Gas Chromatograph, Thermo Scientific) containing a capillary column (Carboxen® 1010 PLOT) equipped with a thermal conductivity detector (TCD).

3. Results

3.1 Characterization of Structural Properties

To determine the surface morphology and the elemental distribution of the CuO_x/Ce_yZr₁. $_y$ O₂ catalysts, SEM-EDX mapping was performed (Fig. 2). The surface of the CuO_x/CeO₂ catalyst is relatively smooth compared to other samples (Fig. 2(a)). As the Zr loading increases, the surface of the catalyst became rougher, and more clusters were observed (Fig. 2(b-e)). Furthermore, with the increase in Zr loading, the grain size of CuO_x/Ce_{0.6}Zr_{0.4}O₂, CuO_x/Ce_{0.5}Zr_{0.5}O₂, and CuO_x/ZrO₂ became smaller, and the surface morphology of the catalysts looks to resemble more closely to that of CuO_x/ZrO₂. The elemental mapping results show that copper oxides were well dispersed uniformly for each of the synthesized samples.



 $\label{eq:constraints} \textbf{Figure 2.} \ \ SEM-EDX \ \ analysis \ \ for \ (a) \ \ CuO_x/CeO_2, \ (b) \ \ CuO_x/Ce_{0.9}Zr_{0.1}O_2, \ (c) \ \ CuO_x/Ce_{0.6}Zr_{0.4}O_2, \ (d) \ \ CuO_x/Ce_{0.5}Zr_{0.5}O_2, \ \ and \ \ (e) \ \ CuO_x/ZrO_2.$

The TEM results demonstrate that the CuO_x species were present on the surface of the respective supports as shown in Fig. 3. Low magnification TEM images for the catalysts are presented in Fig. 3(a-e), where particle overlap was observed. To investigate the microstructural

characteristics of the catalyst materials, high magnification TEM images (Fig. 3(a'-e')) were collected. The presence of constituent species (CeO₂, CuO_x, and ZrO₂) in each catalyst was confirmed based on the interplanar distance corresponding to the catalyst's composition. A consistent lattice spacing of ~0.309 nm, corresponding to the (111) plane of CeO₂, was observed in both CuO_x/CeO₂ and CuO_x/CZ catalysts.³⁶ Although the lattice spacing of CeO₂ is expected to be influenced by Zr contents, no noticeable expansion or contraction of CeO₂ lattice was observed in the HR-TEM results. The different types of the dispersed CuO_x species were identified, revealing the presence of CuO (Cu²⁺) and Cu₂O (Cu¹⁺) in CuO_x/CeO₂, CuO_x/CZ and CuO_x/ZrO₂. catalysts, with corresponding lattice spacing of 0.240-0.265 and 0.209-0.220 nm, respectively. 37,38 Lattice fringes for ZrO₂ (0.290-0.298 nm) were detected in all Zr-containing catalysts, except for CuO_x/Ce_{0.9}Zr_{0.1}O₂, where the higher CeO₂ content likely obscured the ZrO₂ fringe patterns.^{39,40} Additionally, the SAED pattern seen in Fig. 3(a") indicates a highly crystalline lattice (dotted pattern) structure for the CeO₂-based catalyst.⁴¹ However, with increasing Zr content into the support, the SAED patterns (Fig. 3(b"-e")) appeared hazy, corroborating the increasing disorder in the catalyst structure.⁴¹

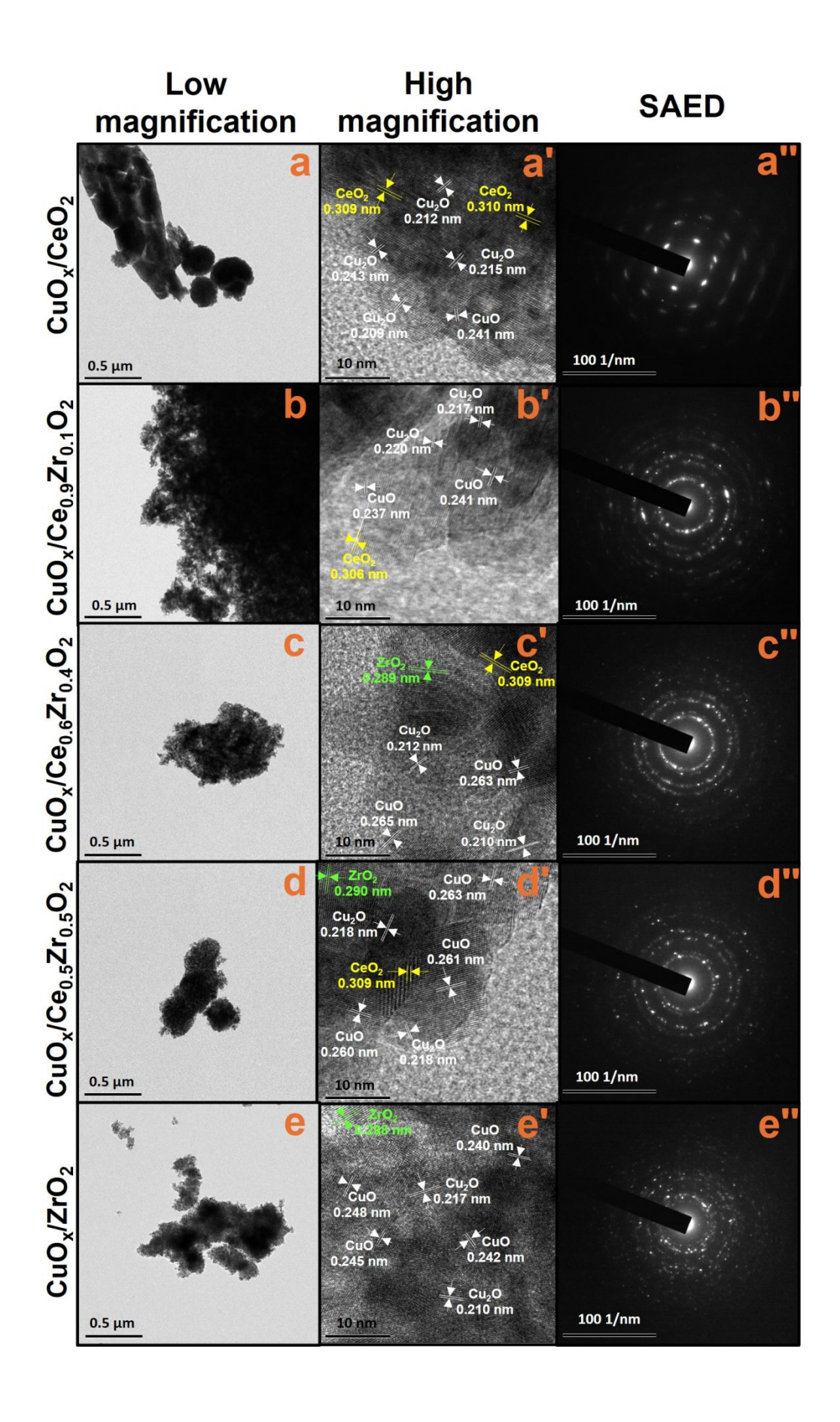


Figure 3. High resolution TEM (HR-TEM) images of synthesized catalysts: (a-a") CuO_x/CeO₂, (b-b") CuO_x/Ce_{0.9}Zr_{0.1}O₂, (c-c") CuO_x/Ce_{0.6}Zr_{0.4}O₂, (d-d") CuO_x/Ce_{0.5}Zr_{0.5}O₂, and (e-e") CuO_x/ZrO₂. High magnification images (a'-e') indicate lattice spacing of metal species (in nm).

The N_2 adsorption and desorption allows for the calculation of the SSA and pore size distribution (or pore volume) of a material. The determined SSA for each of the $Ce_yZr_{1-y}O_2$ supports (Table 1) shows a decreasing SSA with an increase in Zr content, while bulk ZrO_2 contains a higher SSA than that of $Ce_yZr_{1-y}O_2$. In the case of the $CuO_x/Ce_yZr_{1-y}O_2$ supported catalysts' SSA, a similar trend can also be observed. Since the synthesized samples' SSAs were similar to the supports' ones, there is expected to be a minimal change in the surface area following the dispersion and calcination of CuO_x on the support. Based on the pore diameter distributions and the type IV-isotherm curves, it was determined that the synthesized catalysts had a mesoporous structure (Fig. 4(a) and (b)).⁴² It is worth noting that $Ce_{0.9}Zr_{0.1}O_2$ shows very different N_2 -ads-des type with higher pore diameter compared to other $Ce_yZ_{1-y}O_2$. Even if the $Ce_{0.9}Zr_{0.1}O_2$ composition (Ce:Zr molar ratio = 1:0.16) is similar to CeO_2 , the results were not comparable. Furthermore, although $CuO_x/Ce_{0.9}Zr_{0.1}O_2$ sample's SSA value is similar to $CuO_x/Ce_{0.6}Zr_{0.4}O_2$ and $CuO_x/Ce_{0.5}Zr_{0.5}O_2$, its physical properties could be different.

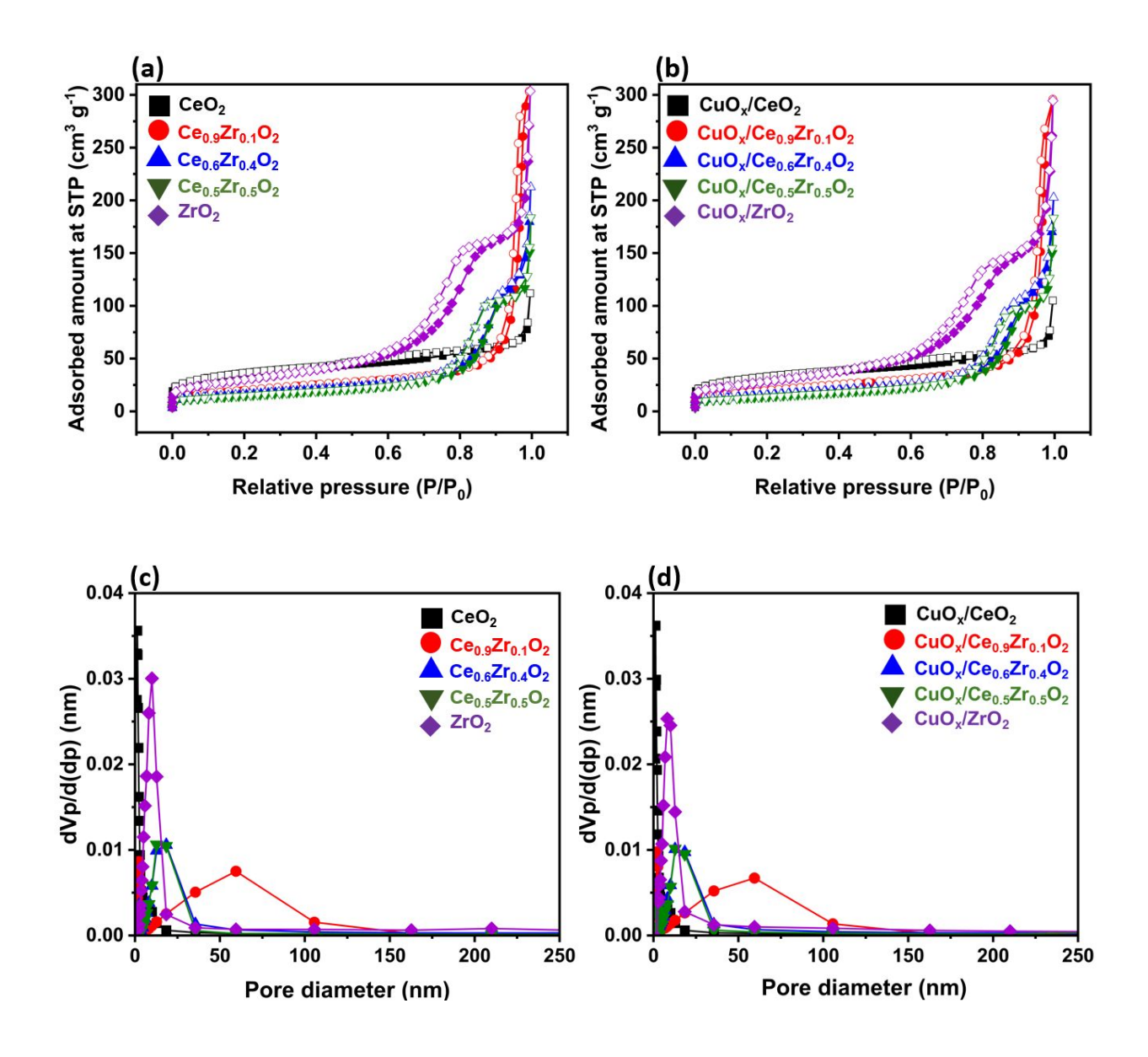


Figure 4. N₂ adsorption and desorption plots for (a) $Ce_yZr_{1-y}O_2(y = 1.0, 0.9, 0.6, 0.5, 0.0)$ supports; and (b) $CuO_x/Ce_yZr_{1-y}O_2$ (y = 1.0, 0.9, 0.6, 0.5, 0.0) catalysts. BJH Pore size distribution for (c) $Ce_yZr_{1-y}O_2(y = 1.0, 0.9, 0.6, 0.5, 0.0)$; and (d) $CuO_x/Ce_yZr_{1-y}O_2(y = 1.0, 0.9, 0.6, 0.5, 0.0)$ catalysts.

Table 1. Specific surface area (SSA) for $Ce_yZr_{1-y}O_2$ (y = 1.0, 0.9, 0.6, 0.5, 0.0) supports and $CuO_x/Ce_yZr_{1-y}O_2$ (y = 1.0, 0.9, 0.6, 0.5, 0.0) catalysts.

Sample (Support)	S_{BET} (m^2/g)	Molar ratio (Ce:Zr)	Sample (Supported)	$S_{ m BET} \ (m^2/g)$
CeO_2	125.7	1:0	CuO _x /CeO ₂	115.1
$Ce_{0.9}Zr_{0.1}O_2$	71.2	1:0.16	$CuO_x/Ce_{0.9}Zr_{0.1}O_2$	70.6
$Ce_{0.6}Zr_{0.4}O_2$	57.1	1:0.92	$CuO_x/Ce_{0.6}Zr_{0.4}O_2$	55.2

$Ce_{0.5}Zr_{0.5}O_2$	53.2	0.72:1	$CuO_x/Ce_{0.5}Zr_{0.5}O_2$	50.0
ZrO_2	108.2	0:1	CuO_x/ZrO_2	101.4

ICP-OES characterization was used to identify the atomic composition of each of the samples and confirm the deposition of Cu on each of the samples. The target SD of Cu for each of the samples was fixed at a value of 2.3 Cu atoms/nm² based on a 3.0 wt% Cu loading basis on pure CeO₂ support. The SD value was initially fixed using the equation:

$$SD\left(\frac{atoms}{nm^2}\right) = \frac{\frac{W_{Cu}}{100}(g) \times 6.02 \times 10^{23} \left(\frac{atoms}{mol}\right) \times \frac{1}{M_{Cu}} \left(\frac{mol}{g}\right)}{SSA_{supp}\left(\frac{m^2}{g}\right) \times \left(1 - \frac{W_{Cu}}{100}\right)(g) \times 10^{18} \left(\frac{nm^2}{m^2}\right)}$$
(1)

where W_{Cu} is the weight loading percent of Cu, M_{Cu} is the molar mass of the Cu (63.5 g/mol), and SSA_{supp} is the SSA of the respective support material (Table 1). The SD of the synthesized catalysts were confirmed using the equation:

$$SD\left(\frac{atoms}{nm^2}\right) = \frac{\frac{W_{Cu}}{100}(g) \times 6.02 \times 10^{23} \left(\frac{atoms}{mol}\right) \times \frac{1}{M_{Cu}} \left(\frac{mol}{g}\right)}{SSA_{synth} \left(\frac{m^2}{g}\right) \times 10^{18} \left(\frac{nm^2}{m^2}\right)}$$
(2)

where the SSA_{syth} is the SSA of the synthesized catalyst (Table 1).

As indicated by Table 2, all samples had comparable SD of ~ 2.0 Cu/nm² indicating controllable Cu precursor adsorption and its dispersion onto each support with varied Cu loadings (e.g., $1.0 \sim 3.0$ wt%). These results also provide that CeO₂, Ce_yZr_{1-y}O₂, and ZrO₂ are effective supporting materials for Cu species' dispersion using the current synthesis method.

Table 2. ICP-OES results with comparison of desired and actual surface densities of catalysts.

Sample	Theoretical Cu loading (wt %)	Actual Cu loading* (wt %)	Theoretical SD (Cu atoms/nm²)	Actual SD** (Cu atoms/nm²)
CuO _x /CeO ₂	3.0	2.6	2.3	2.1

$CuO_x/Ce_{0.9}Zr_{0.1}O_2$	1.7	1.4	2.3	1.9
$CuO_x/Ce_{0.6}Zr_{0.4}O_2$	1.4	1.1	2.3	1.9
$CuO_x/Ce_{0.5}Zr_{0.5}O_2$	1.3	1.0	2.3	1.8
CuO _x /ZrO ₂	2.6	2.1	2.3	2.0

^{*}ICP results, **Applying SSA of the synthesized catalysts from Table 1.

Raman spectroscopy is a powerful analytical tool that provides information about molecular vibrations by measuring the inelastic scattering of light. Visible (532 nm) Raman spectroscopy was used to analyze the Ce_vZr_{1-v}O₂-based support and CuO_x/Ce_vZr_{1-v}O₂ materials and the collected spectra are presented in Fig. S1. For the comparison purpose, CeO2 and ZrO2 Raman spectra were also collected. Please note that the CeO₂ and Ce_vZr_{1-v}O₂ spectra were normalized with respect to the F_{2g} band to better distinguish the formation and relative intensity changing of other peaks (Fig. S1(a)). Bulk ZrO₂ contains peaks at 107, 183, 335, 384, 480, 561, and 615 cm⁻¹ Raman shift, representing the monoclinic phase of zirconia.⁴³ For CeO₂, Ce_{0.9}Zr_{0.1}O₂, $Ce_{0.6}Zr_{0.4}O_2$ and $Ce_{0.5}Zr_{0.5}O_2$, their Raman spectra show a high intensity peak at ~463 cm⁻¹, which is ascribed to the F_{2g} vibration due to the fluorite-type lattice structure of the varying CeO₂-based samples. 44-48 As the Zr content increases, the F_{2g} peak was slightly shifted to a higher Raman shift (or blue shift) from 463 cm⁻¹ to 467 cm⁻¹. Since Zr⁴⁺ has smaller ionic radius than Ce⁴⁺, the Zr-O bonding is shorter and stronger than Ce-O bonding, causing contraction in the structure resulting in a blue shift.⁴³ In addition to a peak shift, Ce_{0.6}Zr_{0.4}O₂ and Ce_{0.5}Zr_{0.5}O₂ show a relatively broadened F_{2g} peak shape compared to CeO₂ and Ce_{0.9}Zr_{0.1}O₂ peaks due to the contribution of the 480 cm⁻¹ Zr peak. Moreover, the presence of a peak in the 141 cm⁻¹ and 144 cm⁻¹ in the bulk support as well as CuO_x/Ce_{0.6}Zr_{0.4}O₂ and CuO_x/Ce_{0.5}Zr_{0.5}O₂ (Fig. S1(b)), respectively, indicates a transition of the ZrO₂ structure from monoclinic (m) to tetragonal (t) due to the incorporation of a larger amount of Zr in the CeO₂ lattice. 49,50 This is followed by a broad peak in the 500-620 cm⁻¹ ranges, indicating the changes of extrinsic (D_{ex}) and intrinsic (D_{in}) defect sites.⁵¹⁻⁵³ It was reported

that intensity variations of D_{ex} and D_{in} are caused by the addition of dopants and changing of inherent structure of the material, respectively. S1-53 This result confirms the increasing of defect sites with increasing Zr loading on CeO₂ structure. In the case of the CuO_x/support samples, the Raman spectra are similar to the bulk support ones, indicating a well-dispersed Cu surface species on the respective supports. Please note that CuO_x Raman peaks, which appear around the 150, 290-350, and ~600 cm⁻¹ regions in general, were either not observed, or were overlapped by the defect region of the supports. The defect regions, especially for CuO_x/CeO₂ and CuO_x/Ce_{0.9}Zr_{0.1}O₂, exhibit an increase in intensity following the addition of Cu, indicating an increase in defect regions within the structure of the catalyst. Additionally, compared to bulk CeO₂, CuO_x/CeO₂ sample shows the F_{2g} peak's broadness as well as a shift to a lower wavenumber, while other CuO_x/support samples show similar results to their support spectra. This is likely a result of the changes in the CeO₂ lattice due to thermal treatment of the support during CuO_x/CeO₂ synthesis, caused by expansion of the CeO₂ structure.

UV (325 nm) Raman spectroscopy is a particularly useful characterization technique for studying defect sites in catalysts, and the collected data is shown in Fig. 5.63 The UV Raman data shown in Fig. 5(a) indicates the presence of the F_{2g} band of the CeO_2 within the $Ce_yZr_{1-y}O_2$ samples at around 461~467 cm⁻¹. The defects in CeO_2 structure are indicated with peaks at < ~600 cm⁻¹ in both bulk CeO_2 and $Ce_{0.9}Zr_{0.1}O_2$ supports. The CeO_2 defect region can be seen to increase as the Zr ratio increased as well as the disappearance of the F_{2g} band (e.g., $Ce_{0.5}Zr_{0.5}O_2$). ^{64,65} The spectra also show the second order longitudinal optical band (2LO) of CeO_2 at ~1200 cm⁻¹ following the similar trend as the defect peaks as they also experienced a blue shift with increased amounts of Zr in the ratio. The blue shifts in the F_{2g} band as well as increasing of the defect sites with increasing Zr ratio clearly indicate a structural change. ^{66,67} Similar to the visible Raman spectra,

the absence of CuO_x related peaks as shown in Fig. 5(b) of the CuO_x/support samples indicate a well-dispersed Cu surface species on the respective supports.

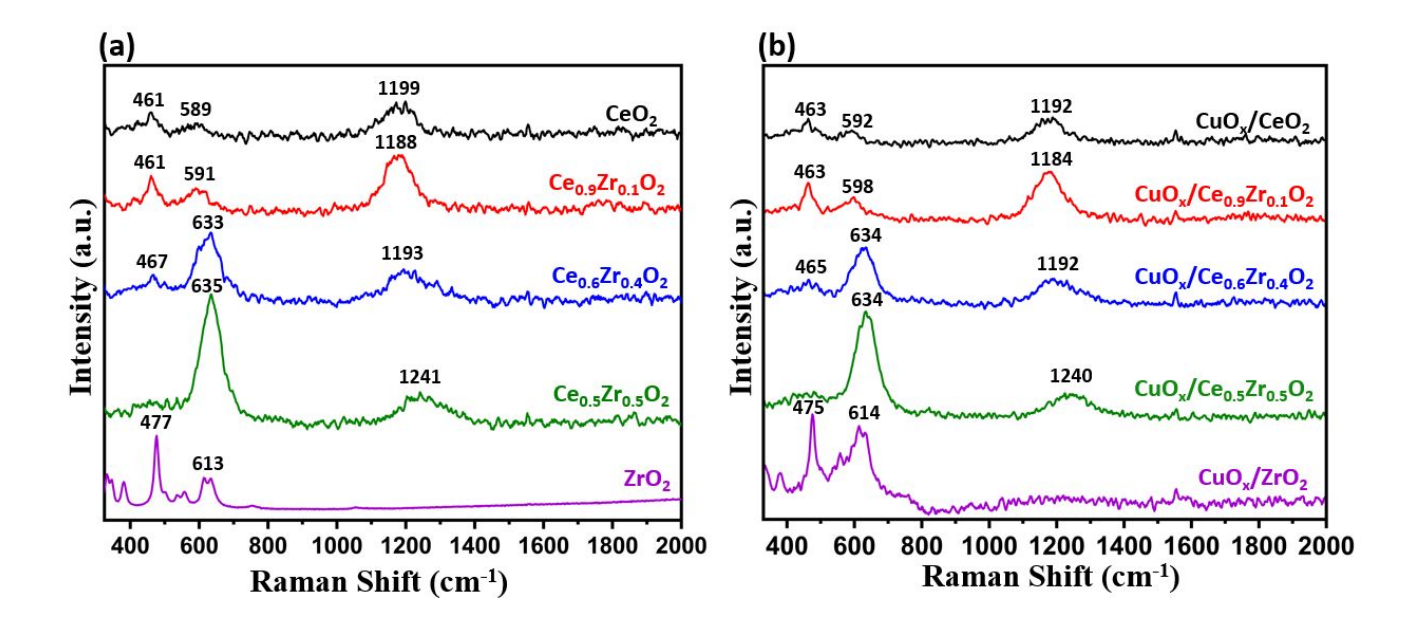
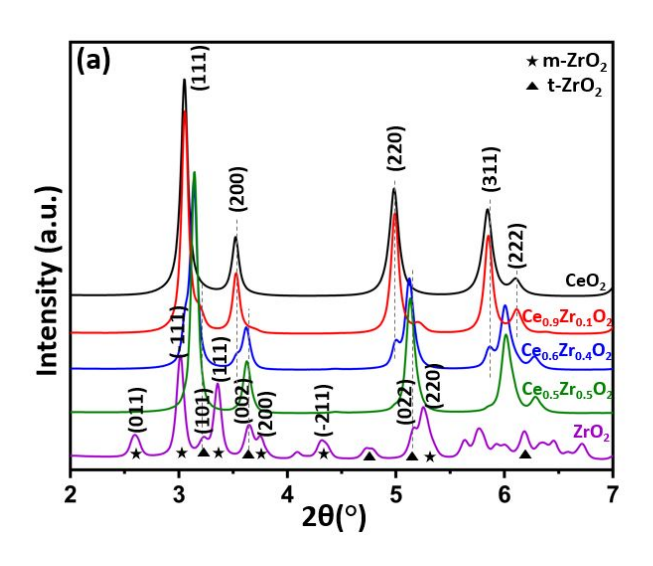


Figure 5. UV ($\lambda = 325$ nm) Raman spectroscopy for (a) $Ce_yZr_{1-y}O_2$ (y = 1.0, 0.9, 0.6, 0.5, 0.0) supports; and (b) $CuO_x/Ce_yZr_{1-y}O_2$ (y = 1.0, 0.9, 0.6, 0.5, 0.0) catalysts.

As shown in Fig. 6(a) and (b), the CuO_x/support samples exhibit the same diffraction peaks as their bulk support counterparts. For comparison purposes, the lab-scale XRD 2θ values were used for labeling throughout the study for structure identification. It should be noted that there are no apparent CuO_x related diffraction 2θ that are corresponding to 36°, 38°, 44.6°, 57.7°, and 68.5° (Fig. 6(b)), indicating that CuO_x surface species was well-dispersed on the synthesized catalysts. This result also provided a minimal deviation in the lattice structure of CuO_x/support materials when compared to the respective supports.⁶⁸⁻⁷¹ The CeO₂ sample showed diffraction peaks at about 28.5°, 33°, 47.5°, 56.4° and 58° with crystal planes corresponding to the (111), (200), (220), (311) and (222) planes, indicating a face-centered cubic (FCC) structure.⁷²⁻⁷⁴ Both the bulk ZrO₂ and CuO_x/ZrO₂ catalyst contain multiphase structure: monoclinic zirconia (m-ZrO₂) at 24°, 28°, 31.5°, 35.1°, 40.7°, 50.2° and tetragonal phase of zirconia (t-ZrO₂) at 30.2°, 34.5°, 45°, 49.4°, 60°.⁷⁵⁻⁷⁹ In

the case of the Ce_vZr_{1-v}O₂ and CuO_x/Ce_vZr_{1-v}O₂ samples, CeO₂ related peaks were slightly shifted to a higher angle, while both Ce_{0.9}Zr_{0.1}O₂-based samples were closest to that of CeO₂-based samples due to the least amount of Ce replacement by Zr in the total ratio. There appears a small shoulder at ~30.2°, indicating the presence of t-ZrO₂ in the Ce_{0.9}Zr_{0.1}O₂ support and CuO_x/Ce_{0.9}Zr_{0.1}O₂ catalyst. Compared to CeO₂ and Ce_{0.9}Zr_{0.1}O₂-based samples, the diffraction peaks of Ce_{0.6}Zr_{0.4}O₂ and CuO_x/Ce_{0.6}Zr_{0.4}O₂ samples were broader, resulting in decreasing a crystallite size (Table 3). In addition to peak broadness, the intensities of CeO₂ peaks decreased, while t-ZrO₂ peaks' intensities were increased. The t-ZrO₂ phase becomes more prominent at higher Zr loading as seen with both Ce_{0.5}Zr_{0.5}O₂ and CuO_x/Ce_{0.5}Zr_{0.5}O₂ samples XRD patterns. Compared to the Ce_{0.6}Zr_{0.4}O₂-based samples, Ce_{0.5}Zr_{0.5}O₂-based samples do not show the peak slitting of CeO₂ (200) in addition to disappearance of the (220) and (311) planes of CeO₂. Crystallite size and lattice parameter calculations were using from the measured XRD data and using equation 3 and 4 (supporting information file). No notable trend of crystallite size can be observed with the change of Ce:Zr ratios as they generally remain in the 10.1–14.1 nm range. However, the lattice parameters were decreased with increasing of Zr content in Ce_vZr_{1-v}O₂ samples due to the smaller size of Zr cation than that of Ce one.



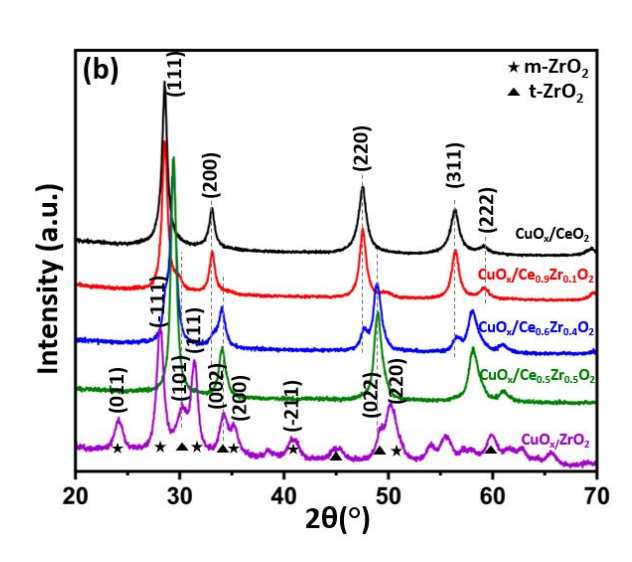


Figure 6. (a) S-XRD spectra for $Ce_yZr_{1-y}O_2$ (y = 1.0, 0.9, 0.6, 0.5, 0.0) supports (λ = 0.1665 Å); and (b) XRD spectra for $CuO_x/Ce_yZr_{1-y}O_2$ (y = 1.0, 0.9, 0.6, 0.5, 0.0) catalysts (λ = 1.54 Å).

Sample	FWHM (°)	Lattice Parameter (Å)	Crystallite Size (nm)
CeO_2	0.074	5.41	11.6
$Ce_{0.9}Zr_{0.1}O_2$	0.071	5.41	12.1
$Ce_{0.6}Zr_{0.4}O_2$	0.076	5.27	11.3
$Ce_{0.5}Zr_{0.5}O_{2}$	0.062	5.25	13.9
ZrO_2	0.080	4.93	10.7
CuO _x /CeO ₂	0.828	5.41	12.3
$CuO_x/Ce_{0.9}Zr_{0.1}O_2$	0.816	5.41	12.2
$CuO_x/Ce_{0.6}Zr_{0.4}O_2$	0.977	5.26	11.1
$CuO_x/Ce_{0.5}Zr_{0.5}O_2$	0.724	5.26	14.1

0.955

CuO_x/ZrO₂

Table 3. Lattice parameter and crystallite size of bulk supports and synthesized catalysts.

The XPS plots of the associated species in $CuO_x/Ce_yZr_{1-y}O_2$ (y=1.0, 0.9, 0.6, 0.5, 0.0) are presented in Fig. 7. The core level Ce 3d spectrum was observed in the 870 – 930 eV range (Fig. 7(a-e) and consisted of Ce $3d_{3/2}$ and Ce $3d_{5/2}$ bands. The Ce 3d spectra observed in CuO_x/CeO_2 , $CuO_x/Ce_{0.9}Zr_{0.1}O_2$, $CuO_x/Ce_{0.6}Zr_{0.4}O_2$ and $CuO_x/Ce_{0.5}Zr_{0.5}O_2$ were deconvoluted into a total of 10 peaks. The peaks (in blue) observed at ~880.1, ~882.5, ~899.2, and ~903.5 eV correspond to Ce^{3+} species. 80,81,82,83 The peaks (in red) observed at ~882.4, ~888.9, ~898.3, ~900.7, ~907.5, and ~916.7 eV attribute to the Ce^{4+} species. 80,81,82,83 The content of Ce^{3+} (relative to Ce^{4+}) was obtained by comparison of their respective peak areas determined by using the equation (3):

4.93

10.1

$$\%[Ce^{3+}] = \frac{[Ce^{3+}]}{[Ce^{3+}] + [Ce^{4+}]}$$
(3)

wherein, $[Ce^{3+}]$ and $[Ce^{4+}]$ are the cumulative peak areas of Ce^{3+} or Ce^{4+} , respectively. 82 As shown in Table 4, the % $[Ce^{3+}]$ values in the CuO_x/CZ samples (0.16~0.19) were slightly higher than in

the CuO_x/CeO₂ sample (0.13), although there was minimal variation with changing Zr concentration. The presence of Cu is confirmed in all CuO_x/Ce_yZr_{1-y}O₂ catalysts with the presence of Cu 2p bands in 920 – 960 eV range. The deconvoluted Cu 2p spectra are presented in Fig. 7 (a'-e'). At a glance, the peaks at ~933.9, ~941.2 and ~953.9 eV are assigned to Cu²⁺ species, while the peaks at ~932.3 and ~952.2 eV correspond to Cu¹⁺ species.^{81,84} To determine the percentage of dominant Cu oxidation state on the catalyst surface, a relative area calculation was performed using equation (4) and the obtained values provided in Table 4.

$$\%[Cu^{1+}] = \frac{[Cu^{1+}]}{[Cu^{1+}] + [Cu^{2+}]} \tag{4}$$

In equation (ii) [Cu¹+] and [Cu²+] are the cumulative peak areas of Cu¹+ or Cu²+, respectively. A decrease in Cu¹+ content was observed in CuO_x/CeO₂, CuO_x/CZ, and CuO_x/ZrO₂ catalysts with increasing Zr concentration, confirming the relationship between Cu oxidation state and the Ce:Zr ratio. Furthermore, the presence of oxygen was observed in all samples with sharp O 1s spectra in the range of 526 – 535 eV range. Fig. 7(a"-e") shows the deconvoluted peaks in O 1s spectrum of samples. The peak that appears at ~528.8 eV represent the lattice oxygen (O') bound to metal species, while peak at ~530.1 eV attributes to loss of oxygen species or creation of oxygen vacancies (defect sites) (O").^{80,85} The area ratio of oxygen related peaks (O"/O') provides insights into the presence of oxygen vacancies in the catalyst. Similar to the %[Ce³+] results, the CuO_x/CZ catalysts (0.83~1.08) exhibited a higher O"/O' ratio than CuO_x/CeO₂ (0.52), indicating a higher presence of oxygen vacancies. The Zr 3d spectra were observed in CuO_x/CZ and CuO_x/ZrO₂ samples in 178 – 188 eV range as shown in Fig. 7(a""-e""). The peaks at ~181.7 and ~184.1 eV for Zr⁴+ were attributed to Zr 3d_{5/2} and Zr 3d_{3/2}, respectively.^{86,87}

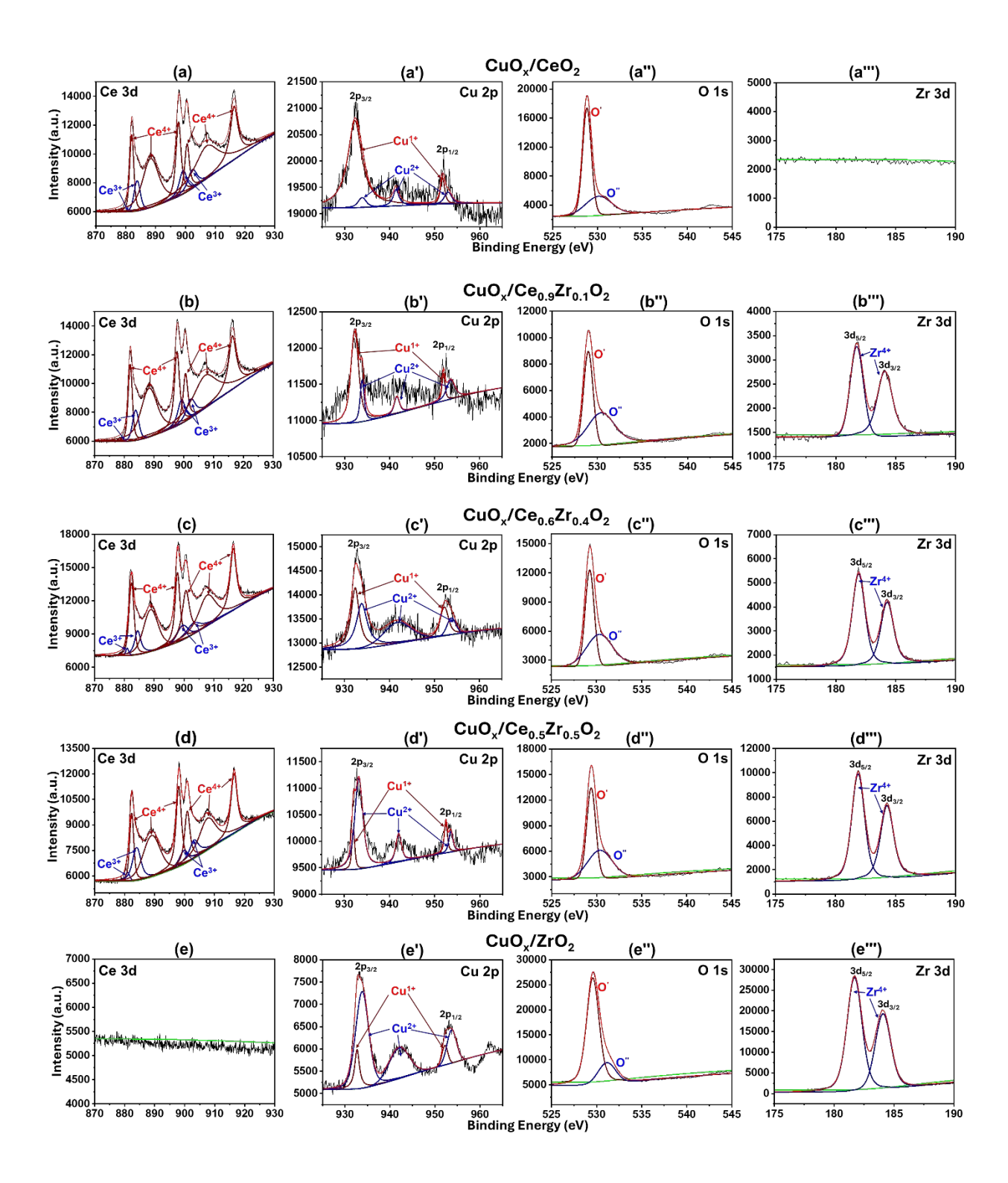


Figure 7. XPS results for $CuO_x/Ce_yZr_{1-y}O_2$ (y= 1, 0.9, 0.6, 0.5, 0) showing deconvolution over (a-e) Ce 3d; (a'-e') Cu 2p; (a"-e") O 1s; and (a"'-e"') Zr 3d spectra.

Table 4. Ce^{3+} area percent, ratio of oxygen vacancies to oxygen in the lattice (O"/O'), and Cu^{1+}

area precent.

Sample	%[Ce ³⁺]	%[Cu ¹⁺]	O''/O'
CuO _x /CeO ₂	0.13	0.84	0.52
CuO _x /Ce _{0.9} Zr _{0.1} O ₂	0.19	0.65	1.08
CuO _x /Ce _{0.6} Zr _{0.4} O ₂	0.16	0.41	0.95
CuO _x /Ce _{0.5} Zr _{0.5} O ₂	0.19	0.19	0.83
CuO _x /ZrO ₂	-	0.14	-

3.2 Catalytic activity testing

Fig. 8 displays the effect of the supports and CO:O₂ feed ratios (e.g., oxygen-rich and stoichiometric conditions) on the CO conversion as a function of temperature. It is evident that CuO_x/CeO_2 and $CuO_x/CeO_9Zr_{014}O_2$ show a higher catalytic performance than other samples under different CO:O₂ ratios based on its T_{20} , T_{50} , and T_{90} values (Fig. 9(a-c), and Table S1). For instance, the CuO_x/CeO_2 and $CuO_x/CeO_9Zr_{0.1}O_2$ catalysts achieved a T_{20} of 51.8°C and 69.3°C, respectively, under CO:O₂ (1:5) conditions, while $CuO_x/CeO_6Zr_{0.4}O_2$ (93.6°C), $CuO_x/CeO_5Zr_{0.5}O_2$ (127.6°C), and CuO_x/ZrO_2 (141.5°C) catalysts show higher T_{20} temperatures under the same reaction conditions. In addition to the support effect, it was also observed that CO:O₂ ratios affect the CO oxidation over the tested catalysts. In the case of CuO_x/CeO_2 and $CuO_x/CeO_9Zr_{0.1}O_2$ catalysts, their catalytic performance was slightly decreased (increasing of T_{20} , T_{50} and T_{90} temperatures) with decreasing O_2/CO ratio ($CO:O_2 = 1:1$ and 1:0.5) (Fig. S2 and Table S1). However, the opposite trend can be seen with the $CuO_x/CeO_0Zr_{0.4}O_0$ and $CuO_x/CeO_0Zr_{0.5}O_0$ catalysts, as their catalytic performance shows an increase with decreasing O_2/CO ratios (Fig. 9(d)). Similar trend was also observed with CuO_x/ZrO_2 catalysts. The $CuO_x/CeO_0Zr_{0.4}O_0$ and $CuO_x/CeO_0Zr_{0.5}O_0$ catalysts

achieved their lowest T_{20} values (88.8°C and 92.2°C, respectively) under stoichiometric (lean O_2) feed conditions. Interestingly, under stoichiometric condition, 100% CO conversion was not achieved as shown in Fig. 8(c), indicating a possible competition between the filling in of oxygen vacancies and the propagation of the reaction. In a short conclusion, for each flow condition, a consistent trend is observed in the sample activity: $CuO_x/CeO_2 > CuO_x/CeO_9Zr_{0.1}O_2 > CuO_x/CeO_9Zr_{0.4}O_2 > CuO_x/CeO_9Zr_{0.5}O_2 > CuO_x/ZrO_2$.

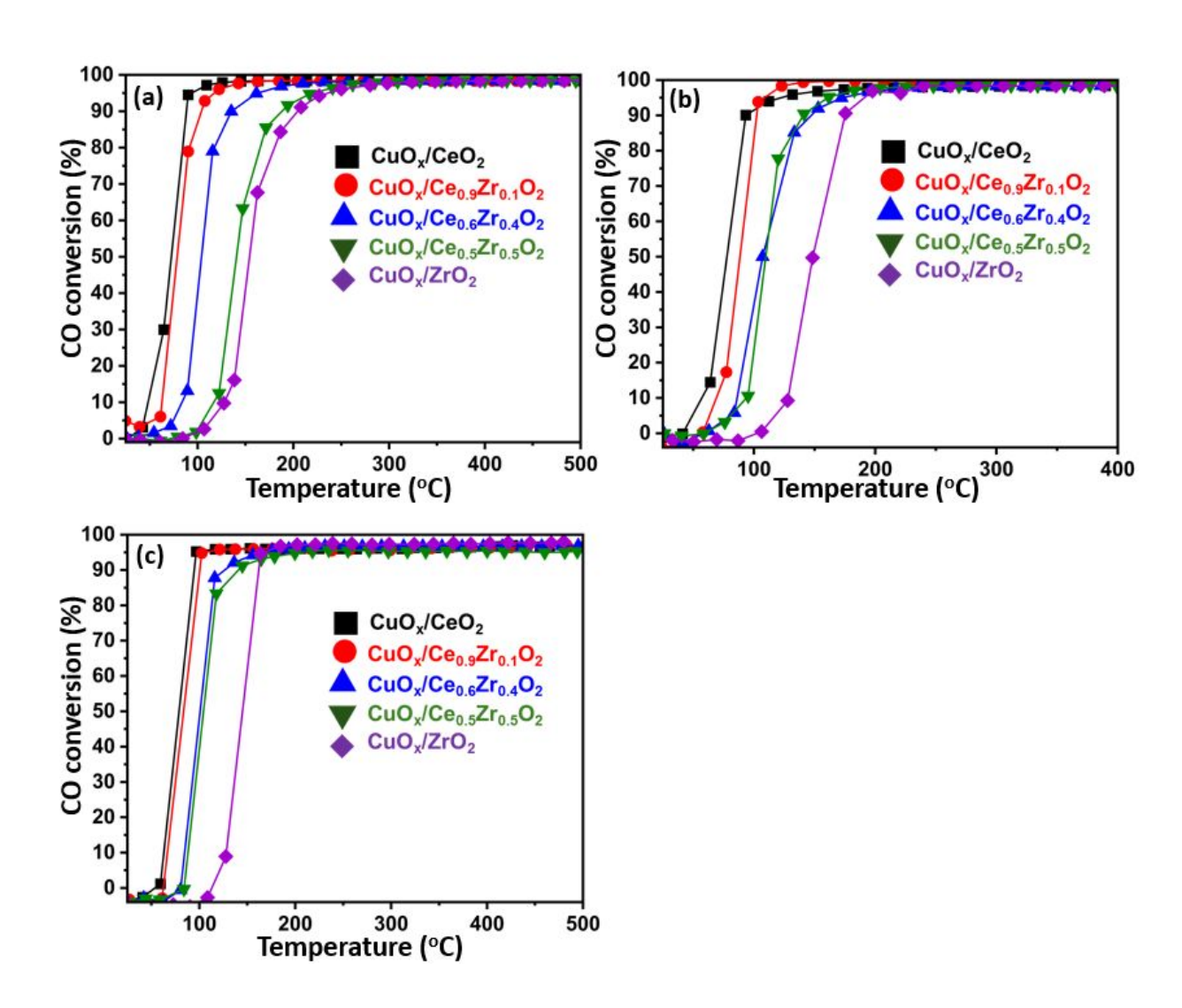


Figure 8. CO oxidation tests over $CuO_x/Ce_yZr_{1-y}O_2$ (y = 1.0, 0.9, 0.6, 0.5, 0.0) catalysts with CO:O₂ feed ratios of (a) 1:5 (b) 1:1 and (c) 1:0.5 (Stoichiometric conditions).

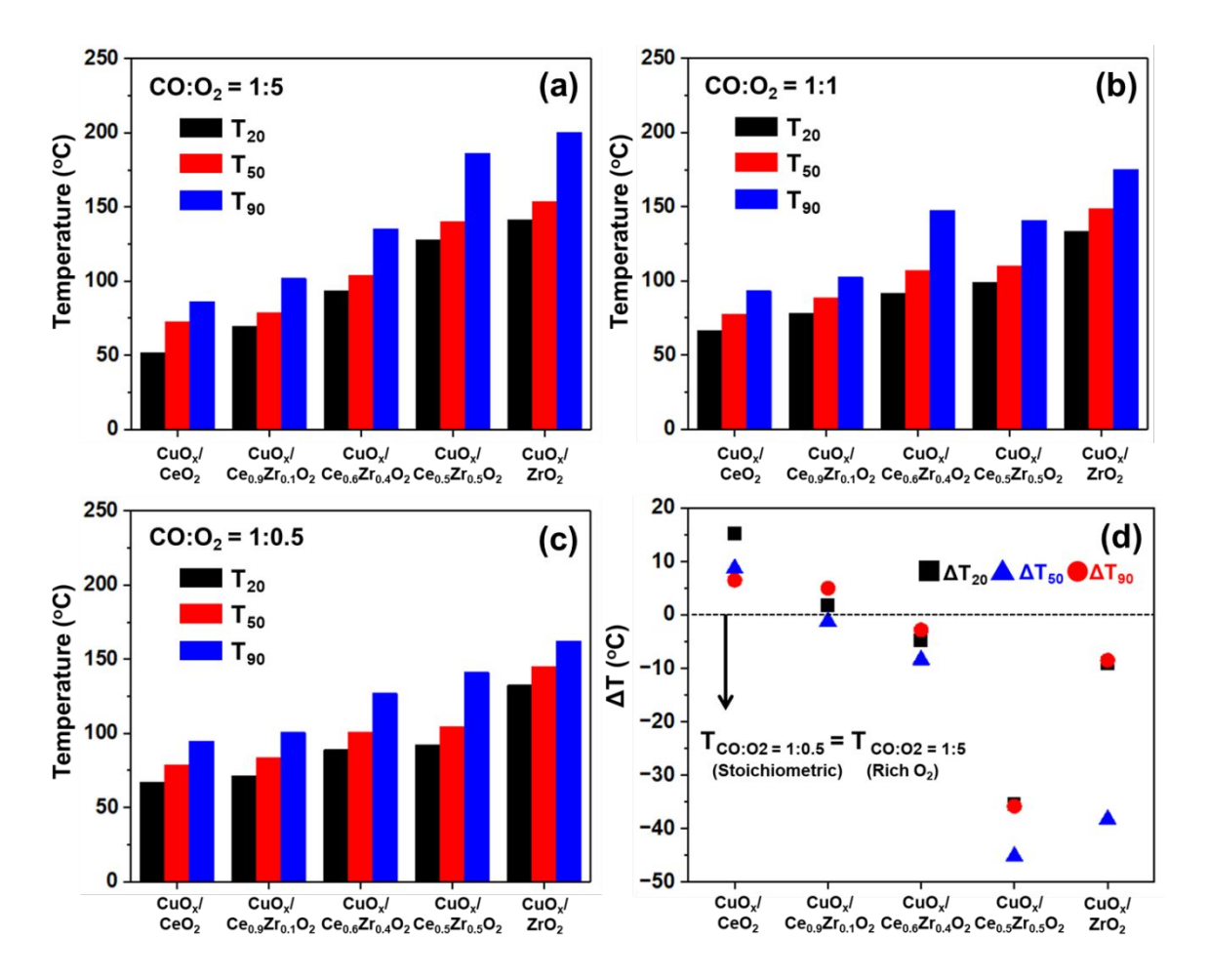


Figure 9. T_{20} , T_{50} , and T_{90} for $CuO_x/Ce_yZr_{1-y}O_2$ (y = 1.0, 0.9, 0.6, 0.5, 0.0) catalysts; $CO:O_2$ feed ratios of (a) 1:5 (b) 1:1 and (c) 1:0.5 (Stoichiometric conditions). (d) ΔT for $CuO_x/Ce_yZr_{1-y}O_2$ catalysts, where $\Delta T = T_{T20, T50, T90 at CO:O_2 = 1:0.5}$ - $T_{T20, T50, T90 at CO:O_2 = 1:5}$.

4. Discussion

4.1. The effect on CeO₂ structure with Zr loading

The incorporation of Zr into the CeO_2 lattice influences the overall structure of the material. The lattice parameters (Table 3) calculated from the XRD plot have a downward trend with increasing Zr loading, indicating that the Zr has been successfully incorporated into the catalyst support structure. The downward trend of the overall lattice parameter for each support as the Zr percentage increases was due to the replacement of Ce^{4+} by a smaller ionic radius Zr^{4+} . $^{22-24,28,43}$ The diffraction peaks of $Ce_{0.5}Zr_{0.5}O_2$ have the relatively highest angle shift as compared to CeO_2

among the diffraction patterns of all different ratio samples due to the highest amount of Ce replacement by Zr in the catalyst structure (Fig. 6(a)). The higher angle shift of the Zr containing Ce_yZr_{1-y}O₂ samples indicates a contraction of the lattice of the material due to increased loading of the Zr.^{22-24,88-90} The appearance of a shoulder near both 5° and 50° in the Ce_{0.6}Zr_{0.4}O₂ respective support and supported catalyst diffraction patterns indicates a transitional state in the ZrO₂structure to a combination of monoclinic and tetragonal phases of CeO₂ and ZrO₂ based on loading ratio.91-94 Additionally, the appearance of a peak at 34.5° corresponding to t-ZrO₂ in the Ce_{0.6}Zr_{0.4}O₂ and Ce_{0.5}Zr_{0.5}O₂ catalysts indicates a shift in the lattice structure of the CeO₂-based catalysts. The UV Raman data (Fig. 5) also indicates a shift in the F_{2g} and 2LO peaks of the samples with increasing Zr loading, which indicates the integration of ZrO₂ into the CeO₂ structure.^{90,95,96} The decrease in the F_{2g} as well as the 2LO band intensity with increasing Zr content can indicate a shift from a CeO₂-dominant structure to a modified CeO₂ structure caused by the contraction of the lattice following the addition of $Zr.^{90,92,95,96}$ Focusing on the F_{2g} band on the visible Raman plot (Fig. S1(a)), it is noted that it shifts closer to the right (blue shift) near the 480 cm⁻¹ peak of m-ZrO₂ with the increasing Zr ratio, confirming a decrease in bond length because of the stronger bond strength of Zr⁴⁺ compared to Ce⁴⁺.97 The reduced bond length further supports the shrink in overall size as indicated by the calculated lattice parameters of the samples (Table 3).88-90 The broad defect band between 500 cm⁻¹ and 620 cm⁻¹ is an indication of increased amounts of extrinsic and intrinsic defect sites on the support, affected by both increasing Zr loading and the addition of a CuO_x dopant (Fig. S1(b)).⁵¹⁻⁵³ For both the bulk and supported Ce_{0.5}Zr_{0.5}O₂ samples, the peaks in the defect range are of higher intensities compared to that of Ce_{0.6}Zr_{0.4}O₂ and Ce_{0.9}Zr_{0.1}O₂, indicating that there is an increase in defect sites within Ce_vZr_{1-v}O₂ catalyst supports at higher Zr loadings. The change in I_D/I_{F2g} ratios (Fig. 10(a)) from the UV Raman spectra of the catalysts

further indicates that the ratio increases with increasing Zr loading, while remaining generally the same between bulk and synthesized catalysts. The intensity of the defects increases while the intensity of the F_{2g} peak decreases indicating increased amounts of defects in the samples with increased Zr loading and the defect peak becoming the dominant. The distinction between extrinsic and intrinsic defects is less clear than in the visible Raman spectra, but the overall presence of defects can be determined by comparison of the loss in ceria's F_{2g} character of the material with increasing defects due to increased addition of Zr into the CeO_2 lattice.

The surface characterization results obtained from XPS measurements were analyzed. While UV Raman, a bulk technique, confirmed the increase in defect sites with increasing Zr content, the surface characteristics from XPS provided further insights. In this context, Ce^{3+} , Cu^{1+} and O" are indicative of the chemistry over the surface of the catalysts. The CuO_x/CeO_2 sample also exhibited the highest %[Cu^{1+}] and lowest %[Ce^{3+}] among the prepared catalysts. As indicated by the O"/O' ratio in Table 4, the inclusion of Zr led to an increase in defect sites. However, the redox equilibrium varied for each catalyst. The generation of Cu^{1+} species (from Cu^{2+}) is driven by the higher electronegativity of Cu compared to Ce, facilitating electron acceptance to attain redox mechanism: $Ce^{3+} + Cu^{2+} \leftrightarrow Cu^{1+} + Ce^{4+}$. The defect sites and oxygen mobility also contribute towards the generation of Ce^{3+} and Cu^{1+} . The authors hypothesize that availability of %[Cu^{1+}] is crucial for oxidation reactions to maximize redox properties.

4.2. The role of oxygen vacancies on activity

As shown by the CO conversion data (Fig. 8), $\text{CuO}_x/\text{CeO}_2$ has the highest performance in oxygen-rich environments due to the innate redox capabilities of Ce^{3+} and Ce^{4+} that increase its oxygen mobility.^{5-7,12-14} With initial fixed SDs of 2.3 Cu atoms/nm², all the synthesized $\text{CuO}_x/\text{Ce}_v\text{Zr}_{1-v}\text{O}_2$ samples have comparable resulting SDs within the range of ~2.0 Cu atoms/nm²,

with the highest resulting SD samples being the catalysts with the highest Ce loading. The slightly higher resulting actual SD values of the CuO_x/CeO₂ and CuO_x/Ce_{0.9}Zr_{0.1}O₂ can be due to the higher SSA of the respective bulk supports compared to the other supports, except for bulk ZrO2 also resulting in an increased overall activity. 75 As shown by Fig. 10(b-d), when normalized by the number of Cu atoms, the highest activity (mol/s/Cu atom), which was obtained at low CO conversion (< 20% CO conversion), is achieved by the CuO_x/CeO₂ and CuO_x/Ce_{0.9}Zr_{0.1}O₂ catalysts. Please note that the near doubling in activity of the catalysts shown in Fig. 10(d) under stoichiometric feed ratios of reactants can be explained by the increase of CO concentration during excess O₂ feed conditions from 4% to 8% to keep the space velocity of the reaction consistent. The relatively low catalytic performance of the CuO_x/ZrO₂ catalyst can be attributed to the lower inherent OSC of ZrO2 and lack of a redox cycle compared to that of CeO2-based materials.21-24 Additionally, an improvement in the performance of Zr-based catalysts can be seen with increasing Ce loading due to improved acid-base support properties compared to that of a pure ZrO₂ support.²¹⁻²⁴ This allows for the proceeding of the reaction with ample optimized interactions with the support. The catalysts achieved a lower final conversion value of ~97% at stochiometric feed ratios (seen in Fig. 8(c)) due to the competing between O2 and CO reactants in the feed and filling in of produced vacancies in the lattice, resulting in O₂ becoming the limiting reactant.^{34-35,98} As such, both the CuO_x/CeO₂ and CuO_x/Ce_{0.9}Zr_{0.1}O₂ catalysts obtained the highest relative conversions under low temperature conditions with varied feed conditions.

To further account for the difference in catalytic activity between the catalysts with a relatively constant number of Cu active sites, the role of oxygen vacancies within the structures of each catalyst during the reaction must be considered. As shown by the CO oxidation activity tests at various excess O₂-feed conditions, oxygen vacancies seem to have less of a role as increasingly

excess O₂ reactants can lead to the vacancies becoming filled in by the excess of oxygen in the reactant stream. 9,13,14,21,35,96,98 The catalytic ability of the synthesized catalysts is therefore dependent on the nature of the support and the SSA of the catalyst, as well as availability of active sites. In this case, pure CuO_x/CeO₂ has a significantly larger surface area compared to the other supports, resulting in more active copper sites even similar SD condition (Table 1 and 2) and leading to better overall conversion at lower temperatures. In contrast, increasing content of Zr in the support leads to a shift in the CO conversion temperatures to the higher temperatures, indicating an increase in the relative T_{20} , T_{50} and the T_{90} (Fig. 9 and Fig. S2). It could be hypothesized that as the Zr content increases, the catalyst's performance decreases due to a lower surface area and the high rate of the oxygen vacancies refilling during the reaction in the presence of O₂ reactants. 29,35,75 Although the oxygen vacancies in the catalysts increase with higher Zr concentrations in the Ce_vZr_{1-v}O₂ catalyst, these vacancies could serve as (1) adsorption sites for reactants and (2) catalytic activity. In the case of low SSA catalysts, however, especially in oxygenrich conditions, the high kinetics of the filling of these vacancies by O_2 leads to a slow regeneration rate, results in reducing the number of active sites available for CO oxidation. Consequently, CO conversion in high Zr ratio $CuO_x/Ce_vZr_{1-v}O_2$ catalysts (e.g., $CuO_x/Ce_{0.6}Zr_{0.4}O_2$ and CuO_x/Ce_{0.5}Zr_{0.5}O₂) results in lower catalytic performance.^{21,35,96,98} The combination of the lower SSA and the reduction of active sites on the catalyst can explain why the activity of Zr-promoted supported catalysts is lower compared to that of CuO_x/CeO₂. As a result, the oxygen defect sites in Ce_vZr_{1-v}O₂ supported catalysts may not be as efficient as desired, depending on the reactant feed ratios (O2 lean or O2 rich) of the reaction in which they are used. To increase the efficiency of the catalytic reaction, it is important to create a catalyst that satisfies both high SSA and abundant OSC.

As described in section 2.1 and shown in Table 2, the catalyst synthesis was based on calculations for a constant Cu surface density (SD = ~ 2.3 Cu atoms/nm²). Table 2 confirms both the actual Cu loading (wt%) and SD. Previous studies reported that the CO oxidation reaction occurs at the interface between CuO_x and CeO₂ or CeO₂-ZrO₂ support.⁹⁹ In this study, the highest Cu loading was obtained in CuO_x/CeO₂, resulting in greater availability of interfaces, which facilitated CO conversions at lower temperatures. During the reaction, oxygen mobility enhances the metalsupport interaction necessary for continuous redox properties, with oxygen vacancies acting as driving potholes for this movement. As shown in Fig. 5, the inclusion of ZrO₂ creates oxygen vacancies or defects in the catalyst. However, an increase in defects does not always enhance catalytic activity, and the lower oxygen mobility of ZrO₂ compared to CeO₂ may negatively affect catalytic activity. A study by M. Piumetti et al. reveals that an optimal balance Ce and Zr content is necessary in the catalyst to achieve sufficient oxygen mobility and create oxygen vacancies, both of which positively influence CO oxidation and help attain the required activity. 100 A higher availability of oxygen vacancy is not the sole factor contributing to an effective catalytic reaction. As shown in Fig. 8(c) and 9(c), $CuO_x/Ce_{0.9}Zr_{0.1}O_2$ shows comparable activity with a stoichiometric feed ratio, despite having a Cu loading (1.4 wt%) that is nearly half of that in CuO_x/CeO₂ (2.6 wt%). This explains the positive impact of the incorporation of ZrO₂ into the CeO₂ structure. With an increase in the oxygen level in the feed, the activity of CuO_x/CeO₂ and CuO_x/Ce_{0.9}Zr_{0.1}O₂ improved. However, a decrease in activity was observed for CuO_x/Ce_{0.6}Zr_{0.4}O₂, CuO_x/Ce_{0.5}Zr_{0.5}O₂, and CuO_x/ZrO₂ catalysts as the O₂/CO₂ ratio increased in the feed. This behavior could be attributed to two main reasons: structural and mechanistic considerations. Firstly, the structural characterization of $CuO_x/Ce_{0.6}Zr_{0.4}O_2$ and $CuO_x/Ce_{0.5}Zr_{0.5}O_2$ shows an increase in defects as the cerium content decreases. This results in causing reduced oxygen mobility and fewer surface

redox-active centers. The second factor is mechanistic, where CO oxidation primarily occurs through the activation of metal centers by oxygen from the feed, which subsequently adsorbs the gas phase CO for CO₂ formation.¹⁰¹ With increased oxygen in the feed, the adsorption of CO at the activated site becomes less favorable due to the higher concentration of oxygen molecules in the vicinity. As a result, higher temperatures are required for effective CO adsorption and facilitate CO₂ formation. This is validated by Fig. 8 and 9, where the breakthrough and subsequent conversion points were observed at higher temperatures as the O₂:CO ratio increased.

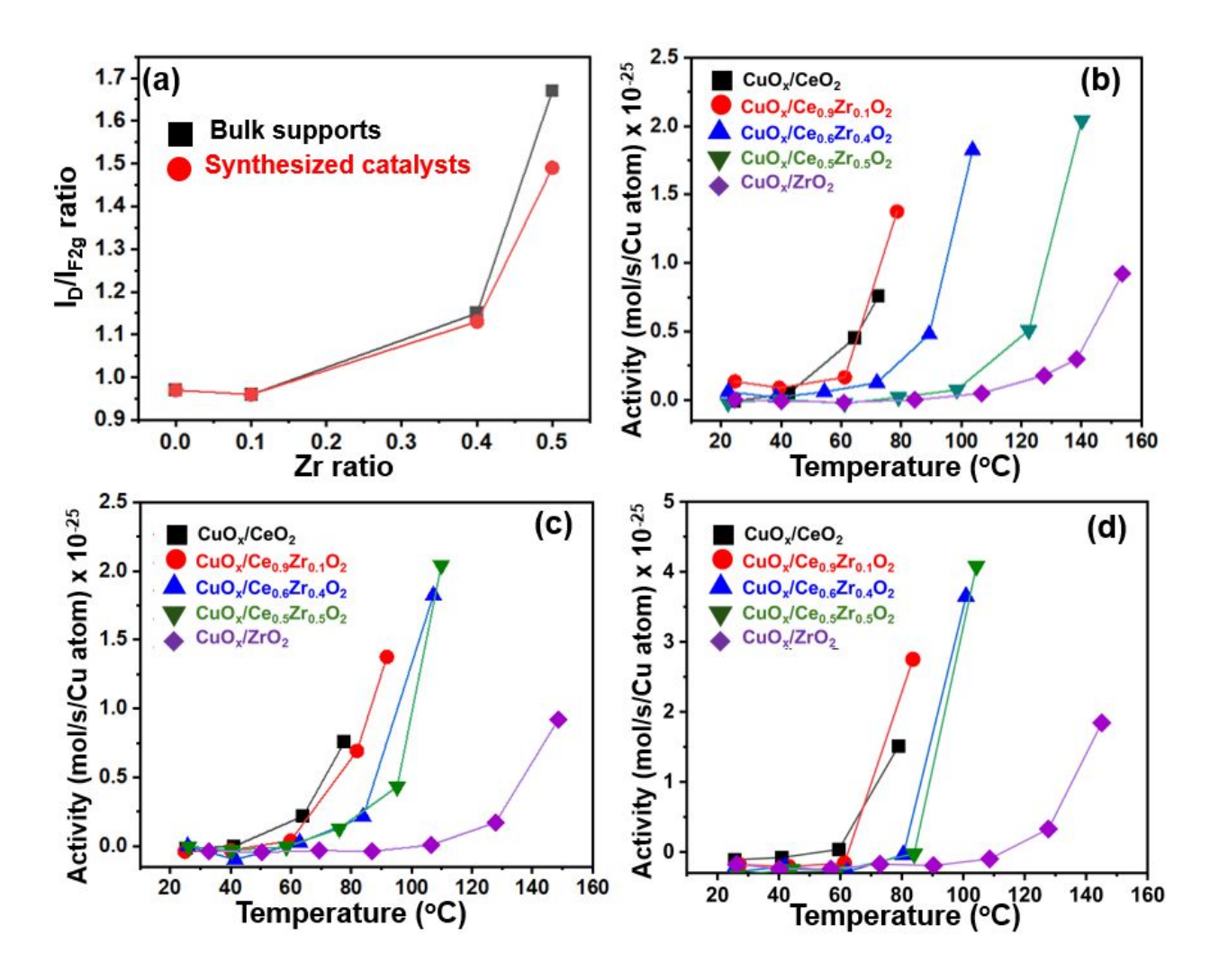


Figure 10. (a) Ratios of the peak intensities of the defect region (I_D) and the F_{2g} mode (I_{F2g}). Activity plots (mol/s/Cu atom) for CO oxidation tests for $CuO_x/Ce_yZr_{1-y}O_2$ (y = 1.0, 0.9, 0.6, 0.5, 0.0) catalysts; The activity plots were calculated for $CuO_x/Ce_yZr_{1-y}O_2$ catalysts undergoing CO

oxidation with CO:O₂ feed ratios of (b) 1:5 (c) 1:1 and (d) 1:0.5 (Stoichiometric conditions) and data displayed up to T₅₀.

The XPS results reveal the presence of the Cu^{1+} and Ce^{3+} species (Fig. 7 and Table 4) in the catalysts correlates with the observed activity results. Higher values of Cu^{+1} and lower values of Ce^{3+} tend to create a gradient that influences the equilibrium mechanism ($Ce^{3+} + Cu^{2+} \leftrightarrow Cu^{1+} + Ce^{4+}$) based on the availability of these species. For example, CuO_x/CeO_2 exhibits a higher concentration of surface Cu^{1+} , which enhances its oxidation capacity. This shift will drive the redox equilibrium backwards upon oxidation, continuously balancing the species throughout the reaction. Consequently, this mechanism is proposed as a source of synergistic effect that enhances CO oxidation performance.

The creation of bulk defects and surface oxygen vacancies has been explained through Raman spectroscopy (Fig. 5 and S1) and XPS analysis (Fig. 7), respectively. Additionally, the presence of lattice distortions was evident from HR-TEM results. The varying electronic states of Cu (Cu¹⁺ and Cu²⁺) were clearly explained in the HR-TEM (Fig. 3) and XPS (Fig. 7) results. The observed results provide that these electronic states contribute to charge-transfer interaction between Cu and the CeO₂-based support's lattice at their interface. 102-104 The presence of Cu¹⁺ can be seen in all but the CuO_x/CeO₂ catalyst, which is in agreement with the presence of a low concentration of Ce³⁺ as shown by the XPS data seen in Fig. 7. The addition of CuO_x increases the reduction-oxidation ability of the support, which is influenced primarily by the composition of the Ce_yZr_{1-y}O₂. This is supported by the inverse relationship observed between the Ce³⁺ and Cu¹⁺ ratios (Table 4). During the CO oxidation reaction, this phenomenon can assist in the adsorption of CO onto the activated CuO_x surface species, which subsequently interacts with lattice oxygen at the metal-support interface, reducing the surface species and creating oxygen vacancies. 103,104 The support composition plays a critical role in determining the type and strength of metal-support

interaction. $^{103-105}$ An et. al., reported that the nature of surface species is key to the effectiveness of metal-support interaction in CO oxidation reaction. $^{103-105}$ Therefore, contribution of metal/metal oxide-support interactions contribute towards increase of the overall active sites for the propagation of the reaction. In this study, the inclusion of Zr up to $\sim 10\%$ constructively contributes to CO oxidation activity. However, the $\text{CuO}_x/\text{CeO}_2$ catalyst showed superior activity among the tested samples, due to its higher metal loading, better redox properties, favorable metal oxide-support interactions, and facilitated oxygen mobility under varying feed conditions.

5. Conclusions

A series of $CuO_x/Ce_yZr_{1-y}O_2$ (y = 1.0, 0.9, 0.6, 0.5, 0.0) catalysts with similar SD (# of Cu atoms/nm²) values were prepared by OP-CVD. The Raman and XRD analysis confirmed that surface CuO_x species were well dispersed on the supports. CuO_x/CeO₂ showed the highest catalytic activity (mol/s/Cu atom) for the CO oxidation reaction, followed by CuO_x/Ce_{0.9}Zr_{0.1}O₂. An improvement in overall CO conversion with higher SSA was observed, even though the number of oxygen defect sites/support showed inverse trends. The effective distribution and presence of CuO_x over Ce_yZr_{1-y}O₂ supports were confirmed from the microstructural data obtained from HR-TEM data. The oxidation states of associated elements in the catalysts were determined using XPS measurements. An indirect quantification of Cu¹⁺, Ce³⁺ and surface oxygen vacancies (O") were analyzed form the deconvolution of the XPS data. The role of oxygen vacancies (both extrinsic and intrinsic) due to the incorporation of a Zr promoter was studied during reaction under varying O₂ feed conditions, in which materials with the highest number of defects performed considerably worse under excess O2 feeds. Under the O2-rich environment, the role of the quantity of metal centers, surface oxygen vacancies, reduction-oxidation ability, metal oxide-support interaction and oxygen mobility play a major role on CO oxidation activity. To further investigate intrinsic

differences of these catalysts and reaction conditions, kinetic experiments for determining activation energy (E_a), pre-exponential factors, rate determining step (RDS) and order of reaction shall be studied separately as an extended scope of this research. To facilitate application in various catalysis industries in addition to fundamental catalysis research, modifications of commercially available supporting materials (e.g., CeO₂ and Ce_yZr_{1-y}O₂) should be thought about. Specifically, synthesizing a high SSA supporting material with high surface oxygen vacant sites and improved oxygen mobility should be taken into consideration.

Data availability

All data included in this study is available on request from the corresponding author.

Conflicts of interest

There are no conflicts of interest to declare.

Acknowledgements

The authors acknowledge funding support from the National Science Foundation (NSF-CBET-2050824). The authors would also like to thank the Advanced Energy Research and Technology Center (AERTC) for the facilities at Stony Brook University. This research used the 28-ID-1 beamline of the National Synchrotron Light Source II, a U.S. Department of Energy (DOE) Office of Science User Facility operated for the DOE Office of Science by Brookhaven National Laboratory under Contract No. DE-SC0012704.

Author Contributions

M. Sifat: Investigation, Formal analysis, Writing – original draft, Writing – review & editing, M. Luchowski: Investigation, Formal analysis, Writing – original draft, Writing – review & editing, A. Pophali: Investigation, Formal analysis, W. Jiang: Investigation, Formal analysis, Writing – original draft, B. Kim: Investigation, Methodology, Formal analysis, G. Kwon: Investigation, Methodology, Formal analysis, K. Yoon: Investigation, Formal analysis, J. Kim: Investigation, Methodology, Formal analysis, K. An: Supervision, S. Shim: Supervision, H. Song: Supervision, T. Kim: Supervision, Writing – original draft, Writing – review & editing, Project administration, Funding acquisition. All authors have given approval to the final version of the manuscript.

References

- 1. D.N. Bateman, *Medicine*, 2003, **31**, 41-42.
- 2. C.L. Townsend, and R.L. Maynard, *Occup. Environ. Med.*, 2002, **59**, 708-711.
- 3. S. Antonaroli, B. Crociani, C. Di Natale, S. Nardis, M. Stefanelli, and R. Paolesse, *Sens. Actuators B*, 2015, **208**, 334-338.
- 4. A. Bhatt, V. Ravi, Y. Zhang, G. Heath, R. Davis, and E. C.D. Tan, *J. Air Waste Manage. Assoc.*, 2023, **73**, 241-257.
- 5. X. Yao, Q. Yu, Z. Ji, Y. Lv, Y. Cao, C. Tang, F. Gao, L. Dong, and Y. Chen, *Appl. Catal.*, *B*, 2013, **130–131**, 293-304.
- 6. L.P. Teh, H.D. Setiabudi, S.N. Timmiati, M.A.A. Aziz, N.H.R. Annuar, and N.N. Rulan, *Chem. Eng. Sci.*, 2021, **242**, 116606.
- 7. K. Yin, S. Mahamulkar, J. Xie, H. Shibata, A. Malek, L. Li, C.W. Jones, P. Agrawal, and R.J. Davis, *Appl. Catal.*, A, 2017, **535**, 17-23.
- 8. A. Longo, L.F. Liotta, G. Pantaleo, F. Giannici, A.M. Venezia, and A. Martorana, *J. Phys. Chem. C*, 2012, **116**, 2960-2966.
- 9. T. Montini, M. Melchionna, M. Monai, and P. Fornasiero, *Chem. Rev. (Washington, DC, U. S.)*, 2016, **116**, 5987-6041.
- 10. P. Ebrahimi, A. Kumar, and M. Khraisheh, 2022, Catalysts, 12, 1101.
- 11. P. Biswas, and D. Kunzru, *Int. J. Hydrogen Energy*, 2007, **32**, 969-980.
- 12. E. Prates da Costa, X. Huang, C. Kübel, X. Cheng, K. Schladitz, A. Hofmann, U. Göbel, and B. M. Smarsly, *Langmuir*, 2023, **39**, 177-191.
- 13. C.R. Jung, J. Han, S.W. Nam, T.-H. Lim, S.A. Hong, and H.I. Lee, *Catal. Today*, 2004, **93-95**, 183-190.
- 14. B. Wang, H. Zhang, W. Xu, X. Li, W. Wang, L. Zhang, Y. Li, Z. Peng, F. Yang, and Z. Liu, *ACS Catal.*, 2020, **10**, 12385-12392.
- 15. S. Nassos, E.E. Svensson, M. Nilsson, M. Boutonnet, and S. Järås, *Appl. Catal., B*, 2006, **64**, 96-102.
- 16. V. Bellière, G. Joorst, O. Stephan, F.M. F. de Groot, and B.M. Weckhuysen, *J. of Phys. Chem. B*, 2006, **110**, 9984-9990.
- 17. Y. Goto, M. Kikugawa, K. Kobayashi, T. Nanba, H. Matsumoto, K. Yamazaki, M. Matsumoto, and H. Imagawa, *Chem. Commun.*, 2022, **58**, 3210-3213.
- 18. T. Kim, J.M. Vohs, and R.J. Gorte, *Ind. Eng. Chem. Res.*, 2006, **45**, 5561-5565.
- 19. G. Balducci, P. Fornasiero, R. Di Monte, J. Kaspar, S. Meriani, and M. Graziani, *Catal. Lett.*, 1995, **33**, 193-200.
- 20. P. Fornasiero, G. Balducci, J. Kašpar, S. Meriani, R. Di Monte, and M. Graziani, *Catal. Today*, 1996, **29**, 47-52.
- 21. P. Li, X. Chen, Y. Li, and J. W. Schwank, Catal. Today, 2019, 327, 90-115.
- 22. H.S. Roh, H.S. Potdar, K.W. Jun, J.W. Kim, and Y.S. Oh, *Appl. Catal.*, *A*, 2004, **276**, 231-239.
- 23. W.S. Dong, K.W. Jun, H.S. Roh, Z.W. Liu, and S.E. Park, Catal. Lett., 2002, 78, 215-222.
- 24. A. Konstandopoulos, C. Pagkoura, S. Lorentzou, and G. Kastrinaki, *SAE Int. J. Engines*, 2016, **9**, 1709-1719.
- 25. D. Duprez, Catal. Today, 2006, 112, 17-22.
- 26. S. Bedrane, C. Descorme, and D. Duprez, Catal. Today, 2002, 73, 233-238.
- 27. I. Iglesias, G. Baronetti, and F. Marino, Solid State Ionics, 2017, 309, 123-129.

- 28. J. Chen, B. Carlson, T. Toops, Z. Li, M. Lance, S. Karakalos, J.S. Choi, and E. Kyriakidou, *Eur. Soc. J. for Cat.*, 2020, **12**, 5558-5568.
- 29. D.W. Lee, S.J. Kim, J. Lee, D. Yoo, Y. Kim, H. Kim, T. Chang, S. Kwon, I. Heo, Y.W. You, and J. Lee, *App. Cat. A.*, 2023, **663**, 119293.
- 30. L. Zhou, X. Li, Z. Yao, Z. Chen, M. Hong, R. Zhu, Y. Liang, and J. Zhao, *Sci. Rep.*, 2016, 6, 23900.
- 31. H.J. Kim, D. Shin, H. Jeong, M.G. Jang, H. Lee, and J.W. Han, *ACS Catal.*, 2020, **10**, 14877-14886.
- 32. H.J. Kim, G. Lee, M. Jang, K.J. Noh., and J.W. Han, *ChemCatChem*, 2019, 11, 2288-2296.
- 33. M. Aryanpour, A. Khetan, and H. Pitsch, ACS Catal., 2013, 3, 1253-1262.
- 34. F. Esch, S. Fabris, L. Zhou, T. Montini, C. Africh, P. Fornasiero, G. Comelli, and R. Rosei, *Sci.*, 2005, **309**, 752-755.
- 35. A. Davo-Quinonero, E. Bailon-Garcia, S. Lopez-Rodriguez, J. Juan-Juan, D. Lozano-Castello,
- M. Garcia-Melchor, F. Herrera, E. Pellegrin, C. Escudero, and A. Bueno-Lopez, *ACS Catal.*, 2020, **10**, 6532-6545.
- 36. S. Soni, N. Chouhan, R.K. Meena, S. Kumar, B. Dalela, M. Mishra, R.M. Meena, G. Gupta, S. Kumar, P.A. Alvi, and S. Dalela, *Global Challenges*, 2019, **3**, 1800090.
- 37. L. Wang, K. Zhang, Z. Hu, W. Duan, F. Cheng, and J. Chen, *Nano Res.*, 2014, 7, 199-208.
- 38. P.C. Rath, J. Patra, D. Saikia, M. Mishra, J.K. Chang, and H.M. Kao, *J. Mat. Chem A*, 2016, 4, 14222-14233.
- 39. C. Colbea, D. Avram, B. Cojocaru, R. Negrea, C. Ghica, V.G. Kessler, G.A. Seisenbaeva, V. Parvulescu, and C. Tiseanu, *Nanomaterials*, 2018, **8**, 988.
- 40. C.C. Chen, W.Y. Cheng, S.Y. Lu, Y.F. Lin, Y.J. Hsu, K.S. Chang, and K.L. Tung, *CrystEngComm*, 2010, **12**, 3664-3669.
- 41. A. Pophali, S. Singh, and N. Verma, *Int. J. Hydrogen Energy*, 2020, **45**, 25985-25995.
- 42. P.M.V. Raja and A.R. Barron, Physical methods in chemistry and nanoscience, 2024, **2**, 55840. https://chem.libretexts.org/Bookshelves/Analytical_Chemistry/Physical_Methods_in_Chemistry_and_Nano_Science_(Barron)/02%3A_Physical_and_Thermal_Analysis/2.03%3A_BET_Surface_Area_Analysis_of_Nanoparticles
- 43. C. Oliveira, F. Garcia, D. Araujo, J. Macedo, S. Dias, and J. Dias, *Appl. Catal. A: General*, 2012, **413-414**, 292-300.
- 44. L. Liu, B. Liu, L. Dong, J. Zhu, H. Wan, K. Sun, B. Zhao, H. Zhu, L. Dong, and Y. Chen, *Appl. Catal. B: Environmetal*, 2009, **90**, 578-586.
- 45. Z. Wu, M. Li, and S.H. Overbury, J. Catal., 2012, 285, 61-73.
- 46. K. Lee, B. Kim, J. Lee, G. Kwon, K. Yoon, H. Song, K. Min, S. Shim, S. Hwang, and T. Kim, *Catal. Sci. Technol.*, 2024, **14**, 279-292.
- 47. K. Lee, M. Brito, J. DeCoster, K. Linskens, K. Mehdi, W. Lee, E. Kim, H. Kim, G. Kwon, C. Nam, and T. Kim, *Mol. Catal.*, 2022, **528**, 112465.
- 48. K. Lee, G. Kwon, S. Hwang, J.A. Boscoboinik, and T. Kim, *Catal. Sci. Technol.*, 2021, 11, 7850-7865.
- 49. G.A.H. Mekhemer, *Colloids Surf. A*, 1998, **141**, 227-235.
- 50. P.E. Quintard, P. Barbéris, A.P. Mirgorodsky, and T. Merle-Méjean, *J. Am. Ceram. Soc.*, 2004, **85**, 1745–1749.
- 51. T. Kaur, K. Singh, and J. Kolte, J. Phys. Chem. C, 2022, 126, 18018-18028.
- 52. Z. Wang, Y. Gao, Y.J. Chabal, and K. Balkus Jr, Catal. Lett., 2017, 147, 738-744.
- 53. L. Li, F. Chen, J.Q. Lu, and M.F. Luo, *J. Phys. Chem. A*, 2011, **115**, 7972-7977.

- 54. Y. Deng, A.D. Handoko, Y. Du, S. Xi, and B.S. Yeo, ACS Catal., 2016, 6, 2473-2481.
- 55. G. Niaura, *Electrochim. Acta*, 2000, **45**, 3507-3519.
- 56. A. Singhal, M.R. Pai, R. Rao, K.T. Pillai, I. Lieberwirth, and A.K. Tyagi, *Eur. J. Inorg. Chem.* 2013, **2013**, 2640-2651.
- 57. L. Debbichi, M.C. Marco de Lucas, J.F. Pierson, and P.J. Krüger, *J. Phys. Chem. C*, 2012, **116**, 10232-10237.
- 58. W. Wang, Z. Liu, Y. Liu, C. Xu, C. Zheng, and G. Wang, *Appl. Phys. A: Mater. Sci. Process*, 2003, **76**, 417-420.
- 59. N. Kainbayev, M. Sriubas, D. Virbukas, Z. Rutkuniene, K. Bockute, S. Bolegenova, and G. Laukaitis, *Coatings*, 2020, **10**, 432.
- 60. K.C. Anjaneya, J. Manjanna, G.P. Nayaka, V.M. Ashwin Kumar, G. Govindaraj, and K.N. Ganesha, *Physica B: Cond. Matter*, 2014, 447, 51-55.
- 61. V.V. Sal'Nikov, and E. Pikalova, *Phys. Solid State*, 2015, **57**, 1944-1952.
- 62. S. Xu, A. Fan, H. Wang, X. Zhang, and X. Wang, Int. J. Heat Mass Trans., 2020, 154, 119751.
- 63. C. Hess, Chem. Soc. Rev., 2021, **50**, 3519-3564.
- 64. T. Taniguchi, T. Watanabe, N. Sugiyama, A.K. Subramani, H. Wagata, N. Matsushita, and M. Yoshimura, *J. Phys. Chem. C*, 2009, **113**, 19789–19793.
- 65. T. Taniguchi, T. Watanebe, S. Ichinohe, M. Yoshimura, K. Katsumata, K. Okada, and N. Matsushita, *Nanoscale*, 2010, **2**, 1426-1428.
- 66. B.M. Reddy, and A. Khan, Catal. Surv. Asia., 2005, 9, 155-171.
- 67. P.T.A. Campos, C.F. Oliveira, J.P.V. Lima, D.R. de Queiroz Silva, S.C.L. Dias, and J.A. Dias, *J. Solid State Chem.*, 2022, **307**, 122752.
- 68. P. Chakartnarodom, N. Kongkajun, and E.A. Laitila, Key Eng. Mat., 2017, 751, 202-206.
- 69. M.A. Thakar, S.S. Jha, K. Phasinam, R. Manne, Y. Qureshi, and V.V. Hari Babu, *Mater. Today: Proc.*, 2022, **51**, 319-324.
- 70. S. Suresh, S. Karthikeyan, and K. Jayamoorthy, J. Sci.: Adv. Mater. Devices, 2016, 1, 343-350.
- 71. M. Ahamed, H.A. Alhadlaq, M.A. Majeed Khan, P. Karuppiah, and N.A. Al-Dhabi, *J. Nanomater.*, 2014, **2014**, 637858.
- 72. C. Xie, D. Yan, H. Li, S. Du, W. Chen, Y. Wang, Y. Zou, R. Chen, and S. Wang, *ACS Catal.*, 2020, **10**, 11082-11098.
- 73. C. Hu, Z. Zhang, H. Liu, P. Gao, and Z. Wang, *Nanotech.*, 2006, 17, 5983-5987.
- 74. P. Shanmugam, G.P. Kuppuswamy, K. Pushparaj, B. Arumugam, A. Sundaramurthy, and Y. Sivalingam, *J. Mater. Sci.: Mater. Electron.*, 2022, **33**, 9483-9489.
- 75. L. Zhou, X. Li, Z. Yao, Z. Chen, M. Hong, R. Zhu, Y. Liang, and J. Zhao, *Sci. Rep.*, 2016, 6, 23900.
- 76. S. Pengpanich, V. Meeyoo, T. Rirksomboon, and K. Bunyakiat, *Appl. Catal.*, A, 2002, **234**, 221-233.
- 77. L. Kurpaska, *J. Mol. Struct.*, 2018, **1163**, 287-293.
- 78. J. Chen, B.D. Carlson, T.J. Toops, Z. Li, M.J. Lance, S.G. Karakalos, J.S. Choi, and Kyriakidou, *ChemCatChem*, 2020, 12, 5558-5568.
- 79. O. Gorban, I. Danilenko, I. Nosolev, E. Abdullayev, A. Islamov, K. Gavrilenko, A. Doroshkevich, O. Shvets, and S. Kolotilov, *J. Nanopart. Res.*, 2022, **24**, 197.
- 80. K.M. Lee, M. Brito, J. DeCoster, K. Linskens, K. Mehdi, W.I. Lee, E. Kim, H. Kim, G. Kwon, C.-Y. Nam, T. Kim, *Mol. Catal.*, 2022, **528**, 112465.

- 81. C. Deng, Q. Huang, X. Zhu, Q. Hu, W. Su, J. Qian, L. Dong, B. Li, M. Fan, C. Liang, *Appl. Surf. Sci.*, 2016, **389**, 1033-1049.
- 82. T. Naganuma, E. Traversa, *Nanoscale*, 2012, **4**, 4950.
- 83. F. Zhang, P. Wang, J. Koberstein, S. Khalid, and S. Chan, Surf. Sci., 2004, 563,74-82.
- 84. D. Barreca, A. Gasparotto, E. Tondello, Surf. Sci. Spectra, 2007, 14, 41-51.
- 85. M. Ishfaq, M. Rizwan Khan, M. F. Bhopal, F. Nasim, A. Ali, A. S. Bhatti, I. Ahmed, Sunil Bhardwa, and C. Cepe, *J. Appl. Phys.*, 2014, **115**, 174506.
- 86. B.M. Reddy, P.M. Sreekanth, Y. Yamada, Q. Xu, and T. Kobayashi, *Appl. Catal. A: General*, 2002, **228**, 269-278.
- 87. D. Sotiropoulou, and S. Ladas, Surf. Sci., 1998, 408, 182-189.
- 88. M. Park, J. Choi, L. Yang, and H. Lee, Sci. Rep., 2019, 9, 19826.
- 89. J. Mucelini, R. Costa-Amaral, Y. Seminovski, and J.L.F. Da Silva, J. Chem. Phys., 2018, 149, 244702.
- 90. V. Mastelaro, V. Briois, D. Souza, and C. Silva, J. of the Eur. Cer. Soc., 2003, 23, 273-282.
- 91. M. Gateshki, M. Niederberger, A. Deshpande, Y. Ren, and V. Petkov, J. Phys.: Cond. Mat., 2007, 19, 156205.
- 92. M. Kuhn, S.R. Bishop, J.L.M. Rupp, and H.L. Tuller, *Acta Materialia*, 2013, **61**, 4277-4288.
- 93. T. Montini, M. Melchionna, M. Monai, and P. Fornasiero, *Chem. Rev.*, 2016, **116**, 5987-6041.
- 94. A. Trovarelli, and G.J. Hutchings, *Catalysis by Ceria and Related Materials*, Imperial College Press, 2002.
- 95. A. Adamski, P. Legutko, K. Dziadek, K. Parkhomenko, C. Aymonier, V. Sadykov, and A-C. Roger, *E3S Web of Conferences*, EDP Sciences, 2019, **108**.
- 96. C. Andriopoulou, D. Harris, H. Stephenson, A. Efstathiou, and S. Boghosian, *Catalysts*, 2020, **10**, 462.
- 97. I. Dobrosz-Gómez, M.A. Garcia, M.I. Szynkowska, I. Kocemba, and J.M. Rynkowski, *Catal. Today*, 2012, **191**, 142-145.
- 98. S. Wagloehner, D. Reichert, D. Leon-Sorezano, P. Balle, B. Geiger, and S. Kureti, *J. Catal.*, 2008, **260**, 305-314.
- 99. I. Heo, S.J. Schmieg, S.H. Oh, W. Li, C.H.F. Peden, C.H. Kim, and J. Szanyi, *Catal. Sci. Technol.*, 2018, **8**, 1383-1394.
- 100. M. Piumetti, S. Bensaid, D. Fino, and N. Russo, *Appl. Catal. B: Environmental*, 2016, **197**, 35-46.
- 101. S. Wagloehner, D. Reichert, D. Leon-Sorzano, P. Balle, B. Geiger, and S. Kureti, *J. Catal.*, 2008, **260**, 305-314.
- 102. F. Zhao, S. Li, X. Wu, R. Yue, W. Li, X. Zha, Y. Deng, and Y. Chen, Cat., 2019, 9, 256.
- 103. K. An, S. Alayoglu, N. Musselwhite, S. Plamthottam, G. Melaet, A.E. Lindeman, and G. A. Somorjai, *J. Am. Chem. Soc.*, 2013, **135**, 16689-16696.
- 104. D. Kim, D. Park, H.C. Song, B. Jeong, J. Lee, Y. Jung, and J.Y. Park, *ACS Catal.*, 2023, **13**, 5326-5335.
- 105. C.H. Mejia, T.W.V. Deelen, and K.P.D. Jong, *Nat. Comm.*, 2018, **9**, 4459.



October 14, 2024

Data Availability Statement

Ken Taiju

The data that support the findings of the research are available on request from the corresponding author.

Sincerely,

Dr. Tae Jin Kim

Associate professor, Graduate Program Director Materials Science and Chemical Engineering Dept. Stony Brook University, Stony Brook, NY, 11794 Phone: 1-631-632-8433, Fax: 1-631-632-8052

E-mail: taejin.kim@stonybrook.edu